Astronomy & Astrophysics manuscript no. main
April 11, 2018

Systematic search for tidal features around nearby galaxies

I. Enhanced SDSS imaging of the Local Volume

Gustavo Morales[1], David Martínez-Delgado[1], Eva K. Grebel[1],
Andrew P. Cooper[2], Behnam Javanmardi[3] and Arpad Miskolczi[4]

[1] Astronomisches Rechen-Institut, Zentrum für Astronomie der Universität Heidelberg, Mönchhofstr. 12–14, 69120 Heidelberg, Germany
[2] Institute for Computational Cosmology, Durham University, Science Site, South Road, Durham, DH1 3LE, UK
[3] School of Astronomy, Institute for Research in Fundamental Sciences (IPM), Tehran, 19395-5531, Iran
[4] Astronomisches Institut der Ruhr-Universität Bochum, Universitätsstr. 150, D-44780 Bochum, Germany

ABSTRACT

Context. In hierarchical models of galaxy formation, stellar tidal streams are expected around most, if not all, galaxies. Although these features may provide useful diagnostics of the ΛCDM model, their observational properties remain poorly constrained because they are challenging to detect and interpret and have been studied in detail for only a sparse sampling of galaxy population. More quantitative, systematic approaches are required. We advocate statistical analysis of the counts and properties of such features in archival wide-field imaging surveys for a direct comparison against results from numerical simulations.
Aims. We aim to study systematically the frequency of occurrence and other observational properties of tidal features around nearby galaxies. The sample we construct will act as a foundational dataset for statistical comparison with cosmological models of galaxy formation.
Methods. Our approach is based on a visual classification of diffuse features around a volume-limited sample of nearby galaxies, using a post-processing of Sloan Digital Sky Survey (SDSS) imaging optimized for the detection of stellar structure with low surface brightness.
Results. At a limiting surface brightness of 28 mag arcsec^{-2}, 14% of the galaxies in our sample exhibit evidence of diffuse features likely to have arisen from minor merging events. Our technique recovers all previously known streams in our sample and yields a number of new candidates. Consistent with previous studies, coherent arc-like features and shells are the most common type of tidal structures found in this study. We conclude that although some detections are ambiguous and could be corroborated or refuted with deeper imaging, our technique provides a reliable foundation for the statistical analysis of diffuse circumgalactic features in wide-area imaging surveys, and for the identification of targets for follow-up studies.

Key words. Methods: observational – Techniques: image processing – Galaxies: formation – Galaxies: structure – Galaxies: halo

1. Introduction

In the Λ cold dark matter (ΛCDM) cosmogony, structures grow hierarchically under the influence of gravity through numerous mergers of smaller structures consisting mainly of dark matter (DM) (e.g., Press & Schechter 1974; White & Rees 1978; Blumenthal et al. 1984; Davis et al. 1985; Lacey & Cole 1993). Baryonic matter collects in the potential wells of DM halos, then (in sufficiently massive halos) cools and condenses, eventually leading to star formation. State-of-the-art cosmological simulations seek to model the assembly of dark and baryonic mass, star formation, stellar evolution, and so-called 'feedback' processes such as supernovae ab initio in order to demonstrate how complex interactions between these processes give rise to the observed diversity of the cosmic galaxy population (e.g., Kauffmann et al. 1993; Cole et al. 2000; Croton et al. 2006; Vogelsberger et al. 2014; Schaye et al. 2015).

In such models, the stellar content of galaxies forms partly in situ through the condensation of gas in the galaxies themselves, and partly through the accretion of stars tidally stripped from other galaxies that they encounter over cosmic time, which may be partially disrupted or have merged completely by the present day (e.g., Searle & Zinn 1978; Abadi et al. 2006; Purcell et al. 2007). The assembly histories of galaxies with a stellar mass comparable to the mass of the Milky Way vary widely in these models (Guo & White 2008). This is supported by observational results from the detailed study of nearby galaxies. Our Milky Way, for instance, appears to have experienced a relatively quiescent merger history (Hammer et al. 2007), while its neighbor M31 shows a much more extended stellar structure, including a variety of bright stellar streams with different morphologies (e.g., Zucker et al. 2004; McConnachie et al. 2009; Ibata et al. 2014; Thomas et al. 2017).

A well-established prediction is that most of the mass in stellar halos of present-day Milky Way-mass galaxies was contributed more than 9 Gyr ago by a few satellites in the mass range of 10^8 to 10^9 $M_\odot$ (e.g., Bullock & Johnston 2005; De Lucia & Helmi 2008; Cooper et al. 2010; Pillepich et al. 2015; Amorisco 2017b). While stars that formed in situ are expected to dominate the stellar mass profiles of galaxies at small galactocentric radii, accreted stars have a much wider range of binding energies and can give rise to stellar halos extending as far as the virial radius of the host DM halo (e.g., Bullock et al. 2001; Font et al. 2006; Cooper et al. 2013; Rodriguez-Gomez et al. 2016). Long dynamical times in the outer regions of DM halos allow coherent structures formed by tidal stripping, such as streams and shells,

to persist for many gigayears (Johnston et al. 2001). Dynamical friction causes the few most massive satellites to deposit their stars at small galactocentric radii, while the outer regions of stellar halos are more likely to consist of material contributed by a number of less massive satellites (e.g., Bullock & Johnston 2005; Amorisco 2017a). Owing to their low stellar densities and intrinsically low luminosities, it is hard to determine both the full extent of stellar halos and their contributions to the innermost regions of galaxies. Together with other difficulties, this makes it challenging to constrain stellar fractions observationally ex situ (e.g., Cooper et al. 2013; D'Souza et al. 2014; Merritt et al. 2016; Harmsen et al. 2017).

It is more straightforward to detect recent and ongoing accretion events involving satellites that are sufficiently luminous to give rise to bright tidal streams in the outskirts of massive galaxies. A growing number of such features have been detected beyond the Local Group in recent years, and further extragalactic surveys reaching sufficiently low surface brightness have recently been completed or are currently ongoing (e.g., Schweizer & Seitzer 1990; Martínez-Delgado et al. 2007, 2008; Mouhcine & Ibata 2009; Miskolczi et al. 2011; Ludwig et al. 2012; Duc et al. 2015; Okamoto et al. 2015; Merritt et al. 2016; Crnojević et al. 2016; Spavone et al. 2017; Harmsen et al. 2017).

Mergers between galaxies with very different stellar masses (typically mass ratios of around 1:10 or higher) are often called minor mergers. These generally involve long-period orbits, little orbital decay or angular momentum loss for the less massive galaxy (which we refer to hereafter as the 'satellite'), and little disturbance of the central structure of the more massive galaxy. Consequently, thin, coherent stellar tidal streams are a distinctive observable signature of such mergers, more so for less massive, more recently accreted, and kinematically 'colder' satellites (Johnston et al. 2008). Gaseous tidal streams are commonly observed around interacting galaxies and can be easily traced through 21 cm observations. They usually overlap with the stellar features unless, for instance, ram pressure separates them. Gaseous streams may also be detectable in optical data, for example, through their Hα emission or dust content. Pure gaseous streams (such as the trailing Magellanic Stream) are rare, whereas pure stellar streams are more common around massive galaxies following the dispersal of any previously associated gas, or when gas-deficient early-type satellites are disrupted. For a review, see Duc & Renaud (2013). In the case of MW-like hosts, we expect minor merger events to be less frequent in the present-day Universe and the coherent structures they generate (such as tidal tails) to persist only for a few billion years before they become undetectable (Wang et al. 2017). Observationally, however, the frequency with which such streams occur around MW-like hosts and their distribution of morphologies are poorly constrained.

Over the past decade, the Stellar Tidal Stream Survey (STSS) has carried out an ultra-deep, wide-field imaging exploration of several nearby spiral galaxies, based on data taken with amateur robotic telescopes (Martínez-Delgado et al. 2008, 2009, 2010, 2012, 2015). This survey has revealed striking stellar tidal streams of different morphologies with unprecedented depth and detail. Subsequently, Miskolczi et al. (2011) developed a search strategy for low-surface brightness tidal structures around a sample of 474 galaxies in the Sloan Digital Sky Survey (SDSS) Data Release 7 archive (Abazajian et al. 2009). The authors calibrated images taken from the SDSS archive and processed them in an automated manner. Searching for possible tidal streams by visual inspection, they found that at least 6% of their sample showed distinct stream-like features (with a total of 19% presenting faint features of any kind). This study demonstrated that detecting a meaningful sample of tidal features close to the detection limit of the SDSS images is feasible.

Although considerable progress has been made by Miskolczi et al. and other works, studies of structure with low surface brightness in the outskirts of galaxies remain predominantly discovery-driven and qualitative. To enable a meaningful statistical comparison between data with low surface brightness and cosmological models of galaxy formation, two further advances are urgently required: samples with both a well-defined selection function and uniform imaging data, and the development of automated methods to detect and quantify features with low surface brightness.

The majority of existing deep-imaging studies have been targeted at galaxies that are either very nearby or have known features detected in shallower imaging. It is clearly impossible to draw any conclusions about how frequent such features are from these data alone. Furthermore, prior work has focused on structures associated with Milky Way-type galaxies. This definition is subjective; it typically includes galaxies that are sufficiently bright, morphologically regular, and have late Hubble type. Not only does a subjective selection make it harder to compare one observational sample to another, but it is almost impossible to apply a comparable qualitative selection to models. Currently, even the most sophisticated hydrodynamical simulations do not reliably reproduce the full range of morphological details that such judgments are based on. Moreover, selection of Milky Way analogues by qualitative criteria will almost certainly result in a wide sampling of the distribution of fundamental quantities such as stellar mass, and a highly incomplete sample at a given stellar mass. It is much more straightforward, and statistically sound, to carry out comparisons in terms of observable quantities that can be robustly constrained in models, stellar mass being the most obvious choice.

Therefore, to make a meaningful comparison between data and models, deep imaging surveys with simple, quantitative selection functions based on fundamental quantities are necessary. Ideally, these would exploit the statistics of brighter circumgalactic features that can be detected in large samples drawn from shallow wide-area surveys, since the expense of targeted deep imaging is often hard to justify for surveys in which substantial numbers of (statistically important) non-detections are to be expected. Low-surface-brightness features are often said to be ubiquitous, but such statements must take into account the brightness of the features and the depth of the observations. A known (and for a given sample, uniform) limit on depth is crucial to make meaningful statements about counts of structures. Finally, since the role of accretion in the galaxy formation process can be investigated through correlations between structure with low surface brightness and other galaxy properties, it will be necessary to examine large numbers of host galaxies of similar mass without restriction to specific morphologies.

In this work, we take a step toward this more systematic approach by making a statistical assessment of the number of features detected in a survey of a volume-, magnitude-, and size-limited sample of nearby Milky Way-mass (as opposed to Milky Way-type) host galaxies. To keep the study consistent, we select our sample on the basis of mass and recessional velocity. We apply a custom image reduction process uniformly to images of each galaxy in our sample from Data Release 10 of the SDSS (Ahn et al. 2014), reaching a detection limit in surface brightness of approximately 28 mag arcsec^{-2}.

This paper presents our observational results. In subsequent work, they will form the basis of further investigations into the

properties and recent evolution of stellar halos and comparisons with theoretical predictions from ΛCDM models. Stellar halos are believed to have formed through a series of accretion events occurring over the lifetime of their host galaxies. Debris associated with the most ancient mergers and those with intrinsically faint progenitors is likely to have extremely low surface brightness at the present day (below 30 mag arcsec^{-2}). The technique we describe here is therefore well suited to studying evidence for more recent ($t_{\rm lookback} \sim 4-5$ Gyr) interactions and mergers with more massive satellite galaxies, rather than ancient, well-mixed halo components or the contribution of fainter satellites.

Several previous surveys of tidal features have been published, albeit with some key differences in sample selection. Kaviraj (2010) focused on early-type galaxies (ETGs) and found that ∼ 18% of their sample exhibited signs of disturbed morphologies (e.g., shells). This sample was also based on SDSS multiband photometry, but combined with the significantly (∼ 2mag) deeper monochromatic images from the SDSS Stripe 82. Atkinson et al. (2013) studied faint tidal features in galaxies with a wide range of morphologies using the wide-field component of the Canada–France–Hawaii Telescope Legacy Survey. Their sample consisted of 1781 luminous galaxies in the magnitude range $15.5 < r < 17.0$. A classification of tidal features according to their morphology (e.g., streams, shells, and tails) was performed, with no major interpretation in terms of their physical origin, especially when distinguishing between major and minor mergers. They found that about 12% of the galaxies in their sample showed clear tidal features at their highest confidence level. This fraction increased to about 18% when they included systems with weaker tidal features. The colors and stellar masses of central galaxies were found to influence these numbers significantly: linear features, shells, and fans were more likely in galaxies with stellar masses $> 10^{10.5}$ M$_\odot$, and red galaxies were found to be twice more likely to show tidal features than blue galaxies. Table 1 from Atkinson et al. (2013) summarizes an overview of faint substructures studies from earlier work in the literature. We note that no publication attempted a less restricted but still controlled sample, especially focused on a future comparison with state-of-the-art simulations.

Throughout the text, we use the term 'overdensity' to refer to any kind of diffuse feature in the processed image that is not obviously the outward continuation of the brighter isophotes of the host galaxy, without making claims regarding their origin or nature (including whether they are real stellar features or are physically associated with the host galaxy). Minor merger signatures, and more specifically, stellar tidal streams, are understood as a particular class of overdensities, arising from stars distributed around the orbit of a current or former satellite, or else a tidal distortion of the host galaxy. In cases where a host galaxy interacts with a companion of comparable mass (typically referred to as a major merger), both may be severely distorted. Our sample contains very few of these non-equilibrium systems, which we exclude from further consideration.

In Section 2 we describe our sample selection and image post-processing technique. Section 3 presents our results, including the discovery of several new streams and a list of tidal feature candidates for follow-up observations. Section 4 discusses these results and directions for future work. The tables referenced throughout the paper are presented in Appendix A.

2. Data

The aim of this work is to compile a catalog of diffuse overdensities to a known, uniform limiting depth around an approximately volume- and mass-limited sample of host galaxies. This will allow us to constrain the rate of occurrence of tidal debris at the present day and hence (in future work) to test predictions for the frequency and effects of low-redshift minor mergers in galaxy formation models. This section describes how we used the Spitzer Survey of Stellar Structure in Galaxies (S^{4}G, Sheth et al. 2010; Querejeta et al. 2015) to select such a sample of host galaxies, and how we processed the SDSS imaging data for these galaxies in order to search for diffuse overdensities.

2.1. Sample

The S^{4}G is a volume-, magnitude-, and size-limited ($d < 40$ Mpc, $|b| > 30°$, $m_{\rm B_{corr}} < 15.5$, and $D_{25} > 1'$) survey of 2352 galaxies using the Infrared Array Camera (IRAC, Fazio et al. 2004) of the Spitzer Space Telescope (Werner et al. 2004) at 3.6 and 4.5 μm. The azimuthally averaged surface brightness profiles obtained by S^{4}G are typically robust to isophotes at $\mu_{3.6\ \mu m}(AB) \sim 27$ mag arcsec^{-2}, equivalent to a stellar mass surface density of about 1 M$_\odot$ pc^{-2} (Muñoz-Mateos et al. 2015). S^{4}G thus provides an appropriate data set for the study of the distribution of stellar mass and structure in the local Universe, and it is complete for galaxies within the volume relevant to our work and for masses greater than $10^{9.2}$ M$_\odot$, allowing us to select a statistically representative sample of galaxies whose stellar masses have been measured in a uniform manner.

Our work focuses on the frequency of tidal features around galaxies at and above the stellar mass of the Milky Way, because contemporary cosmological volume simulations can readily resolve these galaxies and their brighter satellites, which give rise to the most conspicuous features. We therefore selected elliptical, spiral, and S0 galaxies (according to the morphological type code T given by S^{4}G) with a lower stellar mass limit of 10^{10}M$_\odot$ in the S^{4}G catalog. Constraining the sample in stellar mass limits bias when comparing with simulations, because samples can be selected using equivalent criteria in both. We excluded any galaxies in the region of the Virgo cluster from our parent sample, as defined by the Next Generation Virgo Cluster Survey (NGVS) footprint (Muñoz et al. 2014), in both projected position and line-of-sight distance ($15 < d_{\rm L.O.S.}$ (Mpc) < 18). The study of diffuse circumgalactic structure in dense environments such as Virgo is complicated by additional tidal forces of the cluster potential acting on the host and its satellites. Virgo is a 'rare' system in the context of the volume we study here, and excluding it allowed us to better represent the statistics of lower-mass groups and isolated galaxies. Clusters of mass comparable to Virgo (∼ 10^{14} M$_\odot$) can easily be identified in simulations, so this does not compromise a straightforward model-data comparison. Moreover, 17 known major mergers were removed from the final sample[1]. We note that S^{4}G already excludes targets at low Galactic latitudes ($|b| < 30°$), which is appropriate for our purposes because the detection of features with low surface brightness is severely limited by the presence of extended Galactic cirrus, high extinction, and stellar crowding. Finally, since we used SDSS imaging, we also excluded S^{4}G galaxies outside the SDSS footprint.

We processed the SDSS images of the targets selected from S^{4}G in two individually volume-complete chunks to obtain samples that were feasible for the observing time constraints on

[1] Targets removed as major mergers are NGC 2798, NGC 3166, NGC 3169, NGC 3190, NGC 3227, NGC 3998, NGC 5953, NGC 5954, NGC 4550, NGC 5774, NGC 5775, NGC 3395, NGC 5194, NGC 5195, NGC 4302, NGC 5566, and NGC 5574.

follow-up observations of the robotic telescope network used in the STSS, which prioritizes more nearby galaxies. In this first paper we present the results for a Local Volume sub-sample (galaxies selected with a recession velocity lower than 2000 km/s), comprising a total of 297 galaxies. Figure 1 shows the distribution of the parent sample across the sky in celestial coordinates. As shown later, the distance distribution peaks around 20 Mpc, roughly at the boundary of the Local Volume (Karachentsev & Kashibadze 2006). The stellar mass distribution of the sample is limited to the mass range $10^{10-11}M_{\odot}$, which follows directly from our selection function. Both mass and distance measurements were taken directly from the S^{4}G catalog. Later figures (Section 3) show the sample distribution morphologically and in inclination angle as well.

2.2. SDSS data handling and imaging processing

We used SDSS imaging of the target galaxies selected from S^{4}G in order to search for faint features in their surroundings. The SDSS imaging camera worked in drift-scan mode, opening its shutter for extended periods and imaging a continuous strip of the sky (Gunn et al. 1998). This means that, while not very deep, the SDSS imaging survey was able to deliver data with consistently low systematic variations from field to field and excellent flat-fielding. These conditions are critical when searching for extended, diffuse-light features close to the detection limit. The SDSS imaging data also lie in the optical range and have better angular resolution than those of S^{4}G, which is why the latter was used to select the sample, but not for the discovery of stellar substructures. See Laine et al. (2014) for a comprehensive survey of faint structures in the S^{4}G images.

For each of the 297 target galaxies selected from S^{4}G, we downloaded and reprocessed the available SDSS DR10 imaging archive data. We followed the procedure described by Miskolczi et al. (2011). This consists of four steps: (1) mosaicing of the SDSS images in each bandpass; (2) stacking images in multiple bands to improve the signal-to-noise ratio (S/N), with no weighting applied; (3) two-stage source extraction, including removal of point sources; and (4) Gaussian filtering to enhance features on the scale of interest.

Square mosaics of 30 arcmin (4595 pixels) per side were created in three filters, *g*, *r*, and *i*, using the automatic script in the SDSS Science Archive Server that can be found online[2] (at 20 Mpc, 30 arcmin corresponds to approximately 176 kpc). We used these three filters because they have the highest reported sensitivity, and because their combined transmission curve closely resembles the luminance filters used by other observational works, such as Martínez-Delgado et al. (2010). The mosaics of each filter were then stacked using the IRAF task `imcombine` with the default parameters, in order to improve the S/N of the image. We call this stacked image $I_{\rm gri}$.

Our analysis relies heavily on visual inspection of extended, diffuse features in moderately crowded stellar fields. We therefore processed the stacked images with SExtractor (Bertin & Arnouts 1996) using a two-stage procedure (known as "hot and cold run", Caldwell et al. 2008) in order to remove the majority of unsaturated point sources while preserving regions of diffuse emission. In Step 1, we extracted all sources covering an area of at least 5 pixels at a signficance of 1.5σ and saved a FITS file, I_5, containing these detections (including the central galaxy, which covers a significant fraction of the image). In the second run, the minimum source area was set to 800 pixels ($\approx$ 30 kpc^2 at 20 Mpc), so that only the central galaxy and any other large objects were detected. We call the corresponding FITS file I_{800}. A final image was then created by subtracting I_{800} from I_5, that is, the large-scale source(s) from the total detections. The image resulting from this operation contains only compact sources (mainly stars). We call this image file $I_s = I_5 - I_{800}$. Using the IRAF task `imarith`, the sources previously extracted were subtracted from the original stacked image, that is, $I_* = I_{\rm gri} - I_s$. Thus, I_* is a stacked image with most of the stars in the field masked out, replaced by the average flux of the neighboring pixels.

To enhance the visibility of faint, extended features, we then applied a circularly symmetric Gaussian filter to I_*. Miskolczi et al. (2011) reported that other possible filter types are available in IRAF, including `adaptive` and `hfilter`, which are both based on the Haar-Transform (Fritze et al. 1977). By testing these filters with different settings, they reported that while both are able to enhance faint features, neither is clearly an improvement over Gaussian filtering. A Gaussian filter is then preferred because it is computationally more efficient than other filters. By experimenting with the parameters of the Gaussian filter, they also reported that the best enhancement of faint extended features is achieved with a kernel scale of $\sigma = 7$. We have carried out our own tests and reached similar conclusions, finding that the best compromise between enhancing diffuse structures and preserving image resolution can be found at a σ of 5 to 7 pixels, which at a distance of 20 Mpc corresponds to roughly 2 to 3 kpc. This works because the diffuse features of interest in this study have scales of a few kiloparsecs, therefore removing fluctuations on smaller scales makes them easier to detect by visual inspection. Convolutions with broader kernels take longer to compute without achieving higher detectability. Figure (2) shows an example of the use of this enhancement technique to reveal the giant shell around NGC 4414. Whenever possible, we have added color insets of the central galaxies to the stretched images in order to visualize the relative extent of each galaxy and its low surface brightness halo.

2.3. Photometric calibration and distribution of the surface brightness limit

An important issue for this work is to quantify the depth to which SDSS data allow us to explore faint stellar halo structures. In addition, the mean surface brightness limits of our images must have a narrow distribution to avoid image-to-image variance biasing any statistics we derive from visual inspection. Since the SDSS data were taken over a period of several years, we have to verify that the surface brightness limits of the images of different galaxies do not reflect variations in the quality of flat-fielding and the sky conditions during the observations, such as transparency and lunar phase (we note that SDSS generally observed in dark sky conditions; Eisenstein et al. e.g., 2011; York et al. e.g., 2000; Gunn et al. e.g., 2006). Scattered light due to bright stars in the vicinity of a galaxy will also contribute to fluctuations in depth. Large differences in seeing, depth, and the variance of depth across the image can lead to an important bias in the statistics of faint overdensities in our galaxy sample, since in some cases, non-detections of streams could be due to observational effects.

To quantify this, we measured the surface brightness limit of each image in our sample as follows. First, we performed a photometric calibration to the SDSS *r* band for the coadded images, using the same approach as our previous studies of stellar tidal streams (Chonis et al. 2011) and dwarf satellite galaxy pop-

[2] `dr10.sdss.org/mosaics`

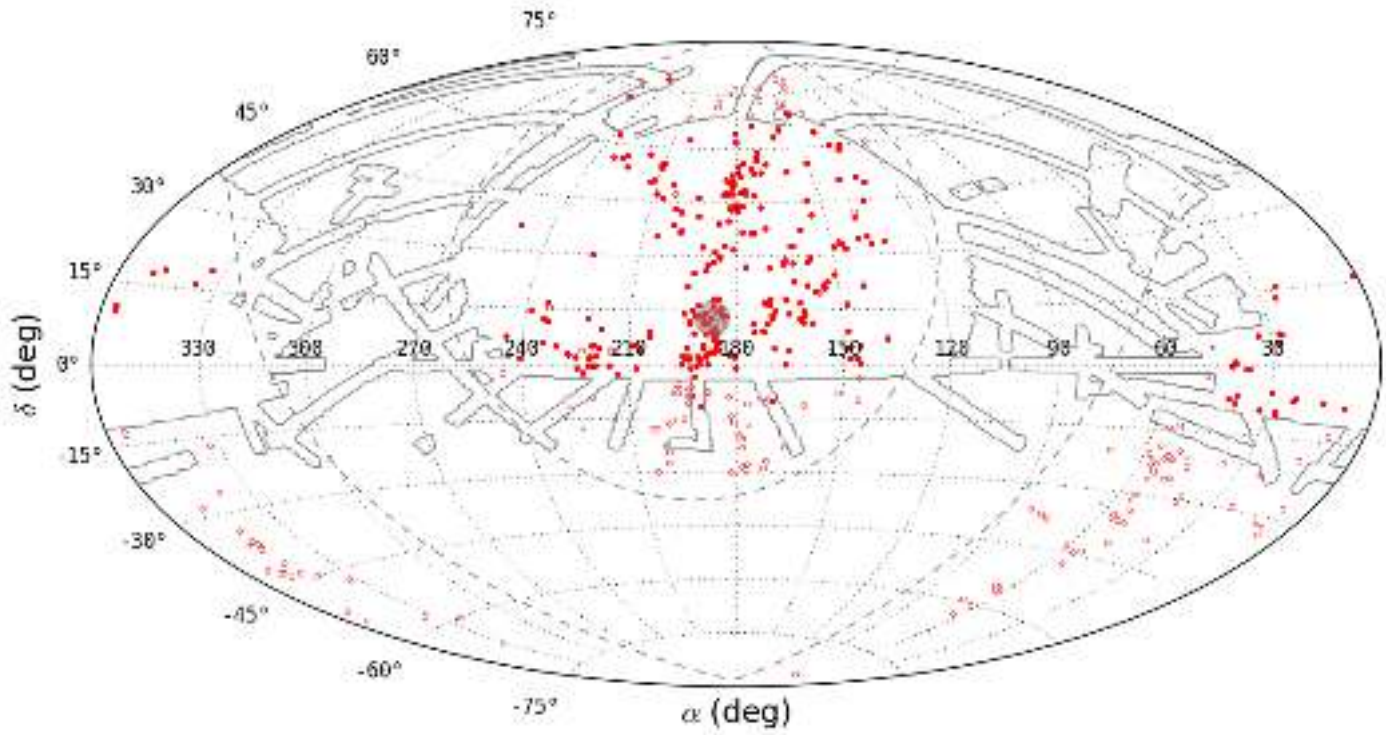

Fig. 1: Aitoff projection of the full S^{4}G catalog (empty and filled red circles). The filled red circles mark our selected parent galaxy sample. The dashed lines enclose the Galactic plane area, the solid gray line encompasses the SDSS DR10 footprint, and the solid gray region encompasses the Virgo Cluster area as defined by the NGVS.

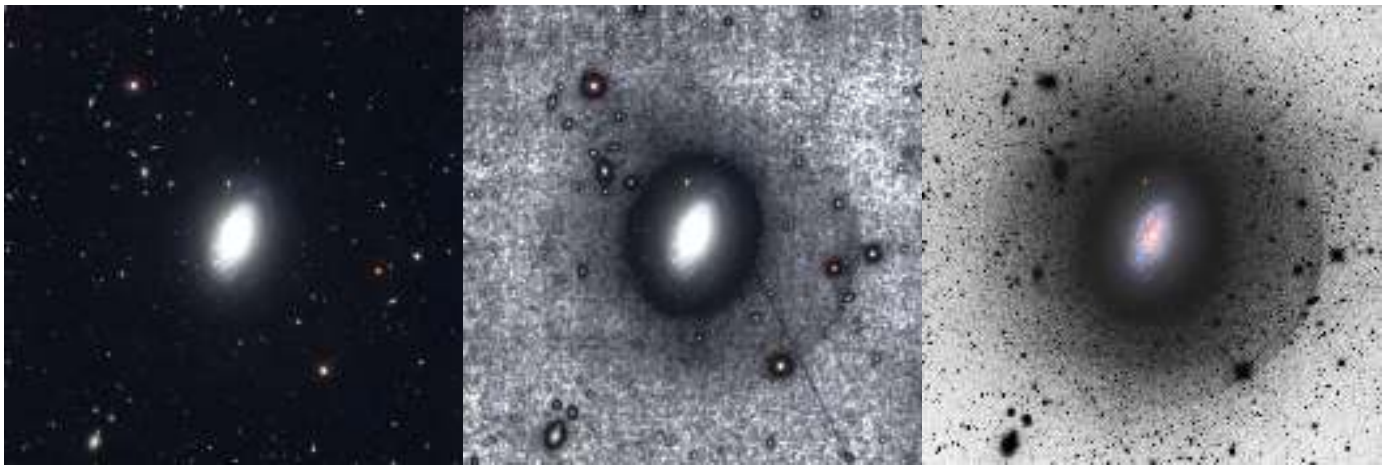

Fig. 2: Example of the enhancement technique described in Sec.2.2 for NGC 4414. The field of view for each panel is ~ 30 × 30 arcminutes (north is up, east to the left). *Left panel*: Original SDSS color-composite image from the public archive. *Middle panel*: Final result of our image processing with an inverted, stretched grayscale showing the extent of a conspicuous shell of debris southwest of the central galaxy. For illustrative purposes, we have added a color inset of the disk of the galaxy and any stars or other objects that are masked in our analysis. *Right panel*: Same field taken from the STSS (Martinez-Delgado et al. in preparation), showing the same overall morphology of this substructure. Credit right panel image: Adam Block.

ulations (Javanmardi et al. 2016). We chose the SDSS *r* band to be consistent with other optical studies. All 297 processed images were calibrated using the semi-automatic pipeline developed (and successfully demonstrated) by the DGSAT[3] project (Javanmardi et al. 2016).

Given the similarity between the effective bandpass of the stacked SDSS images and the wide-band luminance filter (used in the DGSAT), the calibration of our stacked images to the *r* band requires a color correction, taking the form

$$r_{cal} = c_0 \ell_{\rm stacked} + c_1(g - r) + c_2, \quad (1)$$

where r_{cal} is the calibrated *r* magnitude, $\ell_{\rm stacked}$ is the magnitude measured in the 'pseudo-luminance' band of the stacked image, c_0 fixes the linear relation between these two magnitudes, c_1 corrects for a color dependence, and c_2 is the magnitude zero-point

[3] Dwarf Galaxy Survey with Amateur Telescopes

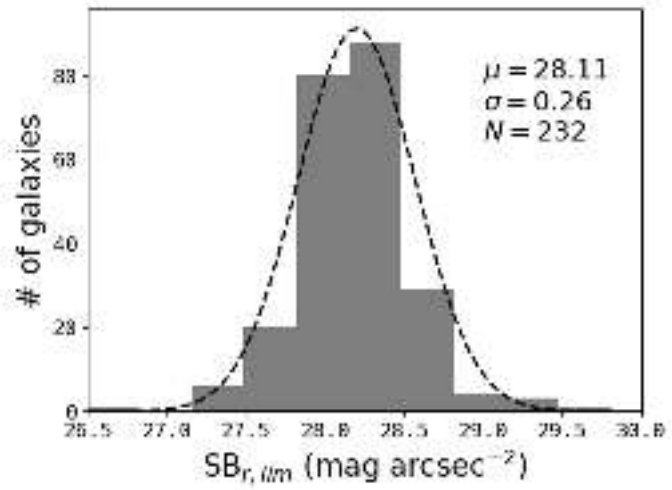

Fig. 3: Distribution of the surface brightness limit in our sample with a Gaussian fit, using the 232 images in the sample with $N_{\rm star} > 50$ stars after the σ clipping as described in Sec. 2.3. We obtained an average value of 28.11, with a standard deviation of 0.26.

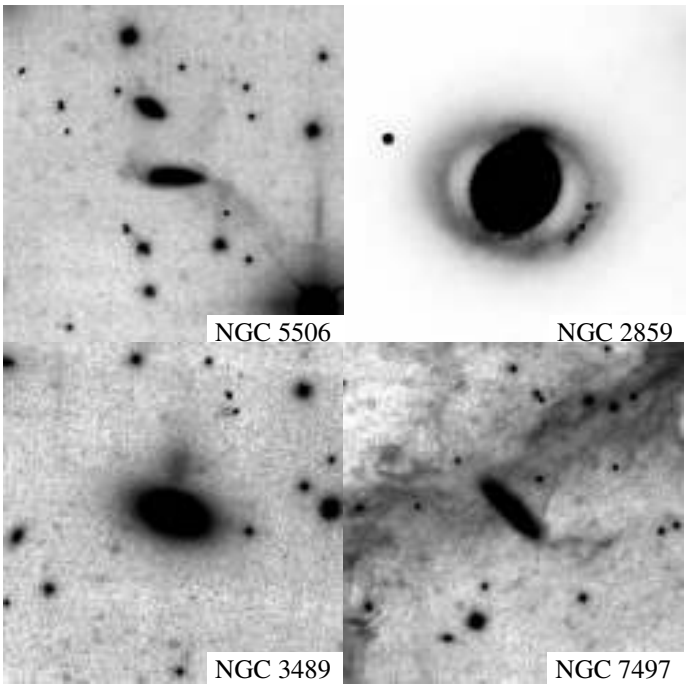

Fig. 4: Examples of very faint diffuse overdensities of different types found during our analysis: i) giant stellar warps of a galactic disk (NGC 5506); ii) a stellar ring with two seemingly interacting, partially disrupted cores embedded in it (NGC 2859); iii) an image artifact resembling a giant satellite (NGC 3489); and iv) extensive Galactic cirrus around NGC 7497. All these images have been processed with our technique, adapted from Miskolczi et al. (2011), using stacked SDSS *g*, *r*, an *i* band images, with a field of view of 30 arcminutes. North is up, east to the left.

correction. The constants c_i are obtained using a set of calibrating stars in each image. These stars are selected using an automated statistical approach (rather than by hand), using the SDSS *g* and *r* band as standard magnitudes.

First, SExtractor (Bertin & Arnouts 1996) was used to detect all the objects in each image. The detected objects were then cross-matched with the most recent SDSS photometric catalog, and only stars with $r \geq 15$, $0.08 < (r-i) < 0.5$ and $0.2 < (g-r) < 1.4$ passed on to the next step (see Chonis & Gaskell 2008). At this point, very many stars are available for calibration of each image. The SDSS r-band magnitudes of the stars were compared iteratively to r_{cal} calculated from each image and the c_i for each stacked image obtained by a χ^2 minimization.

Next, any star with $\Delta r \equiv r_{SDSS} - r_{cal}$ deviating by more than twice the standard deviation σ from the best-fit relation was discarded and the calibration relation was fit again to obtain new c_i. This clipping was repeated until no 2σ outlier remained, which gave us the final c_i for each image. The standard deviation of Δr provides an estimate of the uncertainty in the calibration and is added in quadrature when we report the uncertainty in magnitudes for each image. See Javanmardi et al. (2016) for further details of this approach to photometric calibration.

After calibrating the data set to the SDSS *r* band, the limiting surface brightnesses of our images were determined following the approach described in Martínez-Delgado et al. (2010). In short, to estimate the (residual) sky background, we measured the standard deviation in random sky apertures of 3 arcseconds in diameter and computed the surface brightness corresponding to five times the standard deviation. Figure 3 displays the distribution of the surface brightness limit of all images in our sample due to the mean sky background, showing that the data used in this work are sufficiently homogeneous in terms of quality and depth. We conclude that the mean sky surface brightness limit of our sample in the *r* band is $\mathrm{SB}_{r,lim} \approx 28.1 \pm 0.3$ mag/arcsec^2. This means that for the purposes of the following analysis, we can neglect variations in depth as a significant source of bias in the statistics of low surface brightness features recovered by our visual inspection.

2.4. Deeper follow-up of tidal feature candidates

Although our processed SDSS images reach a surface brightness limit in the *r* band ($\mathrm{SB}_{r,lim}$) that would conventionally be considered 'deep', they are still only deep enough to reveal the brightest structures (if any) in the halos of our target galaxies. In some cases, the low S/N detection of a particular feature and artifacts in the image significantly reduce our confidence in the nature of the detection and/or its interpretation as a signature of tidal disruption. Better (i.e., deeper) data are necessary to improve confidence in these detections.

Figure 4 shows some examples of different types of overdensities found in our search. These illustrate cases in which it is ambiguous whether well-detected overdensities are the result of minor mergers or perturbations of the central galaxy, such as extended stellar warps (e.g., NGC 5506), rings (e.g., NGC 2859) or other tidal distortions (e.g., Trujillo et al. 2009). Significant sky background fluctuations or extended Galactic cirrus (e.g., NGC 7497) are also a well-known problem for the detection of tidal streams (e.g., Duc et al. 2015). Finally, NGC 3489 is a clear example of a typical artifact in the SDSS images, a reflection from a bright star that resembles a diffuse satellite interacting with the central galaxy.

We have explored the availability of deep images for our stream candidates in two separate sources of additional optical data described below. Unfortunately, these additional surveys currently cover a smaller sky area and have fewer bandpasses than the SDSS, and hence are not suitable for the statistical analysis we attempt with SDSS data in this paper.

2.4.1. Stellar Tidal Stream Survey

Figure 5 shows a comparison of our results to the ultra-deep observations of the STSS (Martínez-Delgado et al. 2010) for a set of well-known diffuse features. As found by Miskolczi et al. (2011), the filtering technique we used renders visible in SDSS images the majority of features reported so far by the robotic amateur telescope observations in the STSS pilot survey, although with a lower S/N because of the brighter surface brightness limit of the SDSS. The lower quality of our SDSS data compared to those of Martínez-Delgado et al. (2010) is mainly explained by the short effective exposure times of the individual broadband SDSS observations. This complicates the classification of very faint overdensities, since the lower S/N makes it harder to distinguish actual tidal features from overdensities related to Galactic cirrus or image artifacts. Deeper follow-up observations are necessary to classify these ambiguous detections.

Figure 6 illustrates the benefits of deeper follow-up with observations like those of the STSS for three galaxies in our sample. The first column presents NGC 7743, a galaxy with an apparently clear stellar tidal stream candidate in its outskirts; however, with STSS observations this feature is shown to be (at least predominantly) Galactic cirrus. The second column presents NGC 5750, which shows a remarkable irregular substructure apparently emerging from its disk; deeper STSS observations reveal an additional overdensity on the other side of the galaxy, which is only barely visible at the detection limit of our SDSS images. Finally, the third column presents NGC 3041, in which an arc-like feature is apparent to the north of the galaxy. The amateur telescope data strongly support the interpretation of this feture as a great-circle stream.

2.4.2. Dark Energy Camera Legacy Survey

We have also searched for images of galaxies with visible low surface brightness features (Table A.1) in the optical images from the third data release (DR3) of the Dark Energy Camera Legacy Survey (DECaLS, Blum et al. 2016). This survey uses the Dark Energy Camera (DECam), a wide-field CCD imager at the CTIO Blanco 4 m telescope, to obtain optical imaging covering 14,000 deg^2 in three optical bands (g,r,z). Since the footprint is mostly in the equatorial and southern sky and only a fraction of the DECaLS data have been publicly released, only a few targets have been imaged with sufficient quality and depth to aid in the interpretation of our SDSS images. In the publicly available DECaLS data, we found that three of our targets were imaged in the g, r, and z bands, confirming the detected streams or diffuse-light substructure in the halo from our analysis. Although some sky regions have been imaged in just one DECaLS band so far, we are able to improve our confidence in some low surface brightness features with even these data (see Sec. 3.3). Regarding background subtraction around large objects, it must also be noted that the DECaLS data reduction for large sources has not yet been optimized to the same extent as in the SDSS (Blanton et al. 2011). This explains the rectangular patches in DECaLS images with poor subtraction around large galaxies, which sometimes mimic diffuse galactic structure.

3. Results

3.1. Confidence of detections and morphologies

For all of the galaxies listed in Table A.1, we estimated our confidence in the detection of faint tidal features on a five-point scale, similar to the scheme used by Atkinson et al. (2013). We refer to it as the detection confidence level (DCL), reflecting our certainty that a tidal feature with low surface brightness that is associated with the target galaxy was detected in an image, as follows:

0: No detection of any sort, or high confidence that any candidates are perturbations of the central object (spiral arms, cirrus, etc.).
1: Very uncertain detection of a feature at a S/N too low to judge either the quality of the detection or its tidal nature.
2: Possible detection of a low surface brightness feature, but with low confidence in a tidal origin ($\sim$ 50% certain).
3: Strong detection judged highly likely to be of tidal origin, but without support from any data other than our own.
4: Strong detection where a tidal origin is supported by other data.

In the same table, we also provide an approximate visual classification system for the morphology of the most common features we detect using the following categories, which are not mutually exclusive:

S for classic shells. Disconnected, coherent arcs of material usually concentric with the central galaxy.
C for any coherent, curvilinear features seen in the image (that are not shells). This includes arcs, plumes of debris, and looped structures of gas or stars surrounding their host.
Sph for spheroids and diffuse satellites in the process of disruption, suggestive of very low surface brightness galaxies.
E for extensions of the central galaxy, including but not limited to warps and spiral arms, and some unclassifiable overdensities clearly connected to the disk.
O for any other less common type of features not included above, but suggestive of tidal interactions: fuzzy clouds, spikes, wedges, irregular filaments, etc.

These categories are intended as an simple indication of the appearance of the features we detect. Stronger conclusions about the true physical nature of these features are beyond the scope of this work, and in most cases would require support from techniques other than photometry.

3.2. Sample statistics

By visual inspection of the processed images, we determine that 51 of the 297 galaxies in our sample show either clear or potential signatures of diffuse overdensities in their outskirts above our surface brightness limit (28.1 mag arcsec^{-2}). Table A.1 describe these galaxies and their associated low-surface-brightness features. Of these 51 targets, 28 show overdensities that we judge to be either stellar or gaseous tidal features on the basis of other, deeper observations. A further 23 objects for which we currently lack deeper observations show overdensities that are likely tidal feature candidates (listed in Table A.1 as features with DCL 1 and 2; see Sec. 3.1). Hence a conservative estimate for the frequency with which such features occur in our volume- and mass-limited sample of the local Universe is $\approx$ 9%. This would rise to $\approx$ 17% if all candidates were confirmed by deeper follow-up observations. Considering only previously published features together with the new discoveries reported in this paper, we estimate that $\approx$ 14% of galaxies in the local Universe exhibit diffuse tidal features brighter than 28.1 mag arcsec^{-2} in the SDSS r band. As a reference, all galaxies in our sample that do not show any evidence of diffuse-light structures are listed in Table A.2.

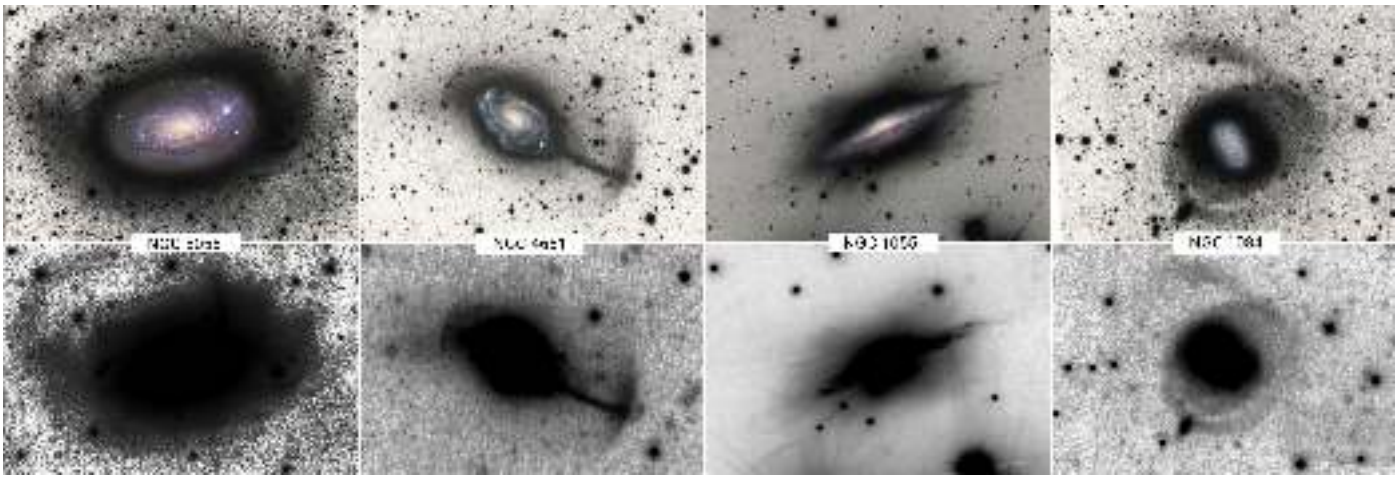

Fig. 5: Comparison between our processed SDSS images and the deep images from the STSS (see Sec. 2.4.1) for the spiral galaxies (from left to right) NGC 5055, NGC 4651, NGC 1055, and NGC 1084. Top row: Images taken from Martínez-Delgado et al. (2010). Bottom row: This work, using SDSS data, after processing as described in Miskolczi et al. (2011), stacking $g-$, $r-$, and i -band images. Even at the shallower depth reached by the SDSS, high-confidence detections can be made with our technique. North is up, east to the left.

Figure 7 shows histograms of our galaxy samples, including the parent sample and subsets of targets that show evidence of tidal streams[4]. Furthermore, it shows that above the surface brightness limit of our sample there are no significant selection effects arising from either morphology or inclination angle, consistent with a roughly isotropic distribution of features. There are some hints of an excess of low surface brightness features at short distance and high stellar mass. The latter is compatible with the expectation of ΛCDM, where more massive galaxies are hosted by more massive DM haloes and are therefore more likely to accrete brighter satellites. Any selection effect with distance is likely to reflect the balance between this effect (large volumes include more bright galaxies) and the increasing difficulty of detecting low surface brightness substructures at larger distances.

We also computed a two-sample Kolmogorov-Smirnov (KS) test to provide a quantitative comparison between the distance, mass, morphology, and inclination angle distributions of the 297 galaxies in our parent sample and those of the hosts of high-confidence tidal feature candidates from Table A.1 (this means a DCL equal to 3 or 4, i.e., a comparison of the black and solid green histograms in Fig. 7). The p-values obtained are shown in Table 1. At a significance of $p = 0.05$, on the basis of any one of these four distributions, we cannot reject the null hypothesis that our sample of galaxies with overdensities is drawn from the same underlying population as the parent sample we selected from S^{4}G. In other words, random sampling from our parent sample has a high probability of yielding distributions similar to those of our sample of galaxies with overdensities.

Variable	p-value
Distance	0.113
Stellar Mass	0.067
Hubble Stage	0.241
Inclination	0.654

Table 1: p-values obtained from a two-sample KS test applied to the histograms depicted in Fig. 7; specifically, the distribution of confirmed tidal streams plus Class I candidates versus the whole sample of 297 galaxies. We cannot reject the hypothesis that the distributions of the two samples are the same.

3.3. Confirmed stellar structures with low surface brightness

Table A.1 lists, among others, the 28 tidal streams that we have confirmed. This list contains 12 unpublished detections, including those found recently in the STSS (Martinez-Delgado et al., in preparation). Figure 8 shows the corresponding images for each of their 12 host galaxies. In these images, the disks of galaxies tend to dominate the field of view because the images have been significantly contrast-stretched to render the low surface brightness structures visible. These new streams are briefly described below. The estimated physical extent of these substructures has been calculated assuming the distance to the target taken from the NASA/IPAC Extragalactic Database (NED). It must be noted that the NED uses the mean value of redshift-independent distances. When no mean distance is reported, the Hubble flow distance is used instead.

NGC 681 is an edge-on disk galaxy with a prominent spheroid surrounded by two clear shells along the major axis, extending to $R = 25$ kpc southwest and $R = 39$ kpc northeast. Other possible arc-like features (concentric around the galaxy $R = 10$ kpc to the south and extending northeast from the south edge of image) are not apparent in DECaLS images (see Fig. 10).

NGC 2775 is an unbarred spiral galaxy showing a prominent ∼ 29 kpc cloudy structure in its halo, reminiscent of a classical shell from Martínez-Delgado et al. (2010).

NGC 3041 shows an arc-like stream with an extent along its longest dimension of ∼ 4 kpc, northeast of the central galaxy. STSS and DECaLS data (Fig. 6) show this feature clearly, but they do not reveal any further detail. This may be the brighter part of a great circle structure similar to the Milky Way Sagittarius stream, but no surviving progenitor is apparent.

[4] Instead of using the mean redshift-independent distances from NED, we here used the Hubble flow distances, cz/H_0, where cz is the recessional velocity, and $H_0 = 75$ km/s/Mpc.

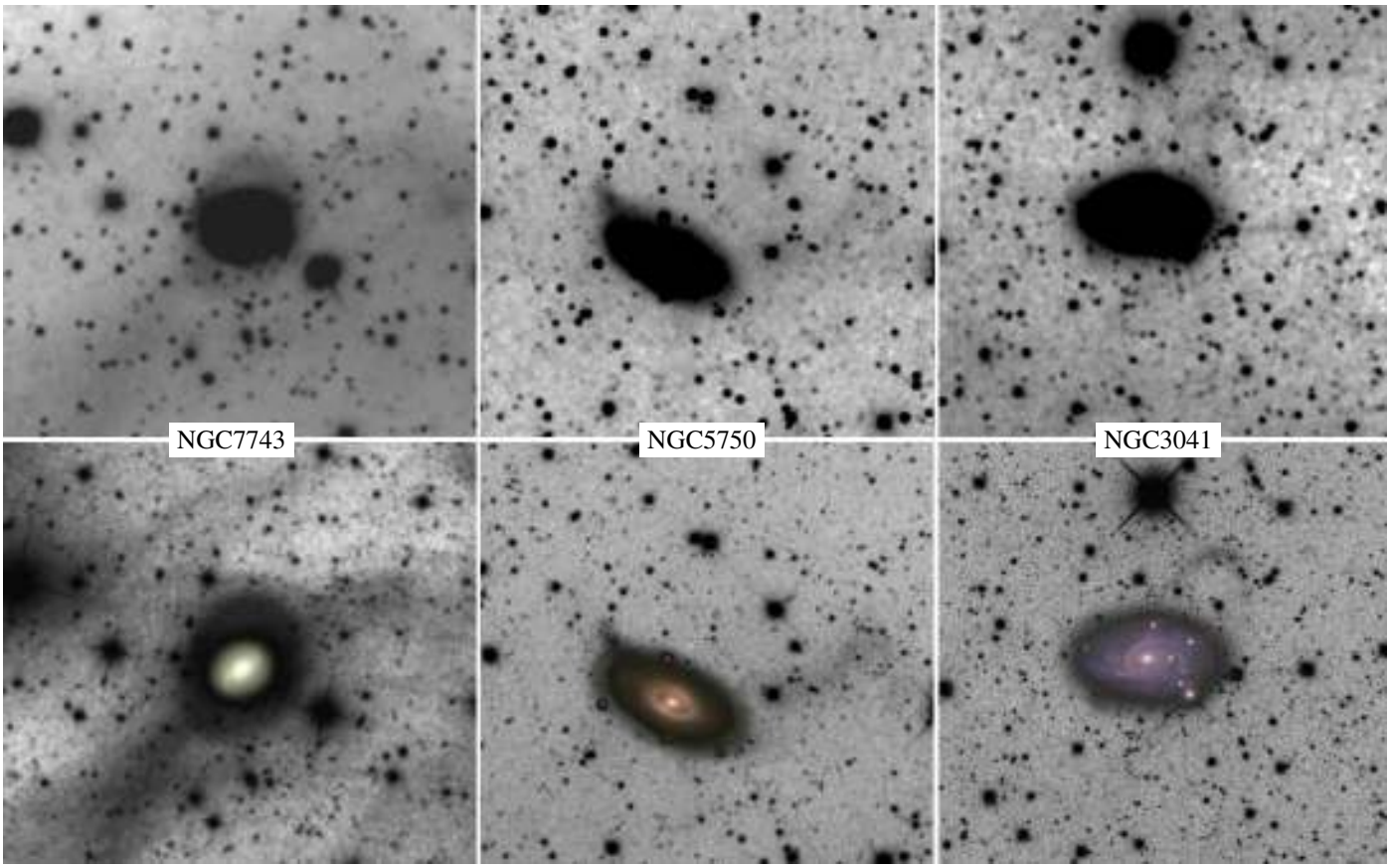

Fig. 6: Examples of some follow-up images used to confirm stellar tidal stream candidates in our sample. The top row shows the SDSS *g-r-i* stacked images for NGC 7743, NGC 5750, and NGC 3041 (see Sec. 3) processed as described in Sec. 2, and kindly provided by A. Miskolczi. The bottom row shows the deep images obtained by the STSS (Martínez-Delgado et al., in prep.) for the same objects, but with a luminance filter. In all cases, the deeper images detect additional features or reveal a more detailed morphology of the features detected in the SDSS images.

NGC 3049 shows an arc-like feature east of the central galaxy, with a size of ∼ 3 kpc. Another very diffuse substructure can be identified to the west, suggestive of a shell formed by tidal disruption. More definitive statements require deeper observations.

NGC 3611 is well known for the peculiar ∼ 30 kpc bright off-center ring-like structure previously noted by Schweizer & Seitzer (1990). These authors favored merging as the origin of this feature, excluding the possibility of a disturbed polar ring. DECaLS data (Fig. 10) show two distinct features: a clear umbrella-like stream with shells on both sides of the galaxy (the most prominent to the east), and an incomplete blue ring or arc encircling the disk. The colors of both structures are clearly different, and it is unclear whether they have a common origin (e.g., the tidal disruption of a Magellanic-type dwarf galaxy).

NGC 3631 shows a giant cloud at a galactocentric distance of ∼ 19 kpc. This is very similar to the M83 stream (Malin & Hadley 1997). It is not clear whether the structure is part of a very faint outer disk or a tidal structure in the galactic halo. This overdensity has also been observed by the STSS (Martinez-Delgado et al., in preparation), indicating that it is not an artifact in the SDSS image.

NGC 3682 shows two classical shells on both sides of the central galaxy, with diameters of ∼ 2 kpc.

NGC 4203 shows a bright, partially disrupted and nucleated satellite southwest of the galaxy, with both a leading and a trailing tail of total length ∼ 13 kpc.

NGC 4569 is a spiral galaxy with a dIrr satellite (IC 3583) to the north, with an apparent interaction between the two[5]. There is evidence of a shell-like overdensity on the northern side of the galaxy, although we cannot reject the possibility that this is an extended warp of the stellar disk.

NGC 4643 shows a clear stellar tidal stream apparently perpendicular to the plane of the galaxy. DECaLS data show evidence for a progenitor in the northern tail. Assuming that both structures apparent in the image are part of the same feature (for example, an arc viewed edge-on), this feature has an extent of ∼ 73 kpc. Whitmore et al. (1990) reported an inner, edge-on arc structure in the main body of the galaxy that is also visible in our images, but not related to the giant tidal structure we report here.

NGC 5750 Both images from our analysis and the STSS deeper images (see Fig. 6) show a truncated overdensity west of the central galaxy, which resembles a faint, distorted satellite galaxy. In addition, an elongated, irregular feature east of the disk (clearly visible in the STSS image) could be part of a tidal stream associated with that satellite.

[5] Although gravitational interaction has been ruled out by some authors (e.g., Boselli et al. 2016).

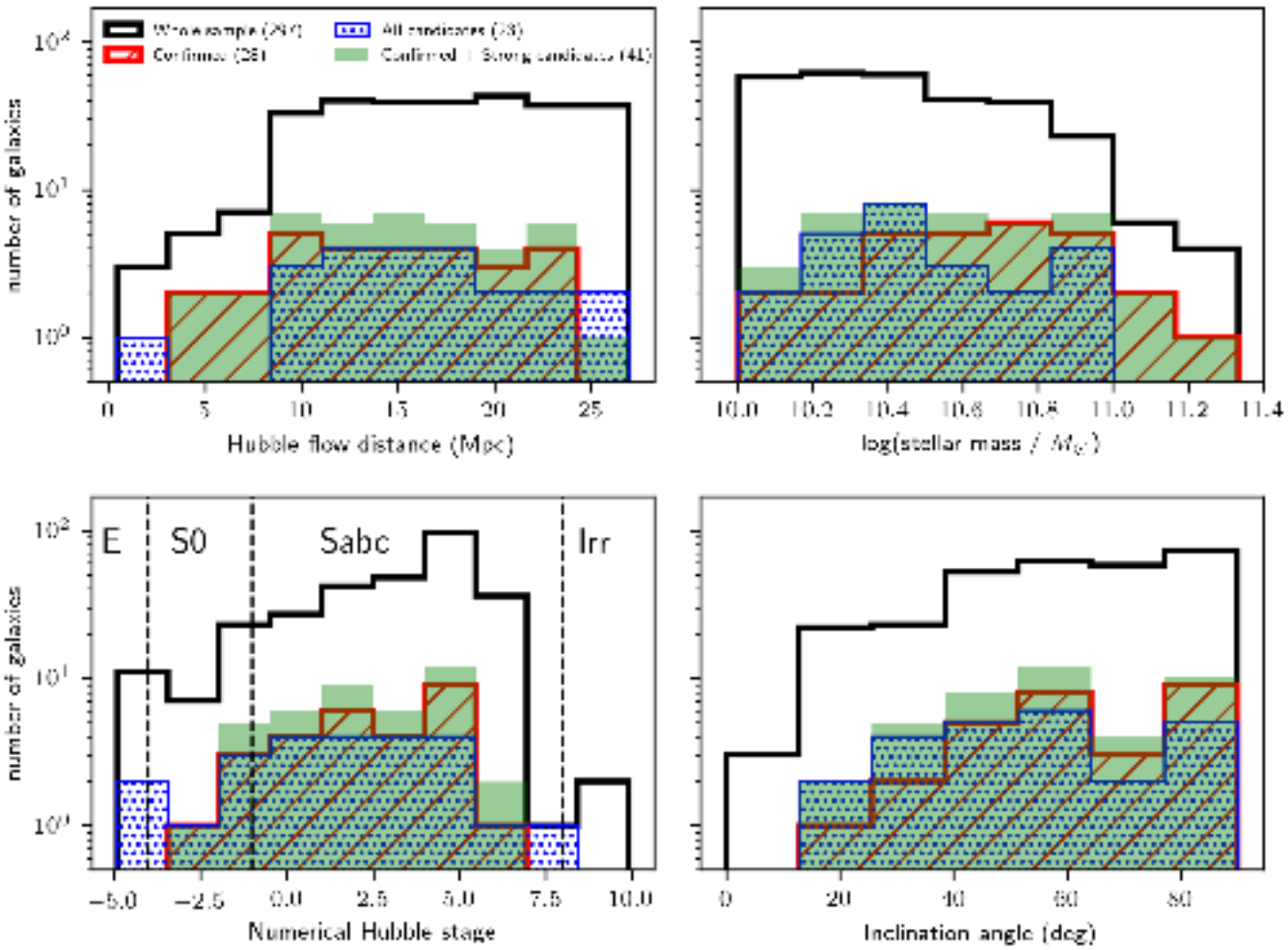

Fig. 7: Histograms of the diffuse-light features found in our whole sample, with or without overdensities, as a function of target distance, stellar mass, morphology and inclination angle. The distribution of all 297 galaxies in our sample is shown in black, while histograms in color correspond to the galaxies listed in Table A.1, our main results. The red distributions represent 28 confirmed features, previously known and new (with a DCL of 4; see Sec. 3.1). Unconfirmed feature candidates (with a DCL of 1 and 2) are represented by blue dotted histograms. Confirmed streams and strong candidates (i.e., every feature with a DLC of 3 or 4) are grouped together in the solid green histogram (41 targets). For our limiting sky surface brightness of 28.1 $\pm$ 0.3 mag arcsec^{-2}, this implies that $\approx$ 14% of the galaxies in the mass and volume limits our parent sample have detectable stellar overdensities in their outskirts. No significant biases are apparent in our sample of galaxies with diffuse overdensities (with respect to the S4G parent sample, black solid line) except for a somewhat flatter distribution of stellar mass and the lack of overdensities for galaxies more distant than 35 Mpc.

NGC 7742 is a face-on unbarred Seyfert spiral galaxy, which shows three very distinct stellar arcs, possibly sections of a shell (or shells), each 16 – 17 kpc in diameter.

NGC 7743 is a barred Seyfert spiral galaxy showing a giant, 18 kpc loop structure to the northeast. Galactic dust clouds dominate the field of view in longer exposures, as shown in the first column of Fig. 6.

3.4. Tidal stream candidates for follow-up studies

Table A.1 lists the galaxies of our sample with detected structures for which a tidal origin cannot be confirmed in this work because we lack deeper data; 23 in total, with a DCL equal to 1 or 2. Follow-up observations of these galaxies are currently being carried out by the STSS and will be published in a forthcoming companion contribution (Martínez-Delgado et al., in preparation). These signatures define those that are very probably stellar tidal streams, that is, tracing orbits of satellites in the tidal field of the host galaxy, and features that are probably linked to disk warping, polar rings, and other types of signatures. In general, any features more likely related to galactic perturbations of the central galaxy disk due to dynamical interaction with other massive galaxies were tagged accordingly. Some examples of these structures of different types are displayed in Fig. 9. Figure 10 shows the images used to confirm the faint tidal debris detected around six of the galaxies listed in Table A.1.

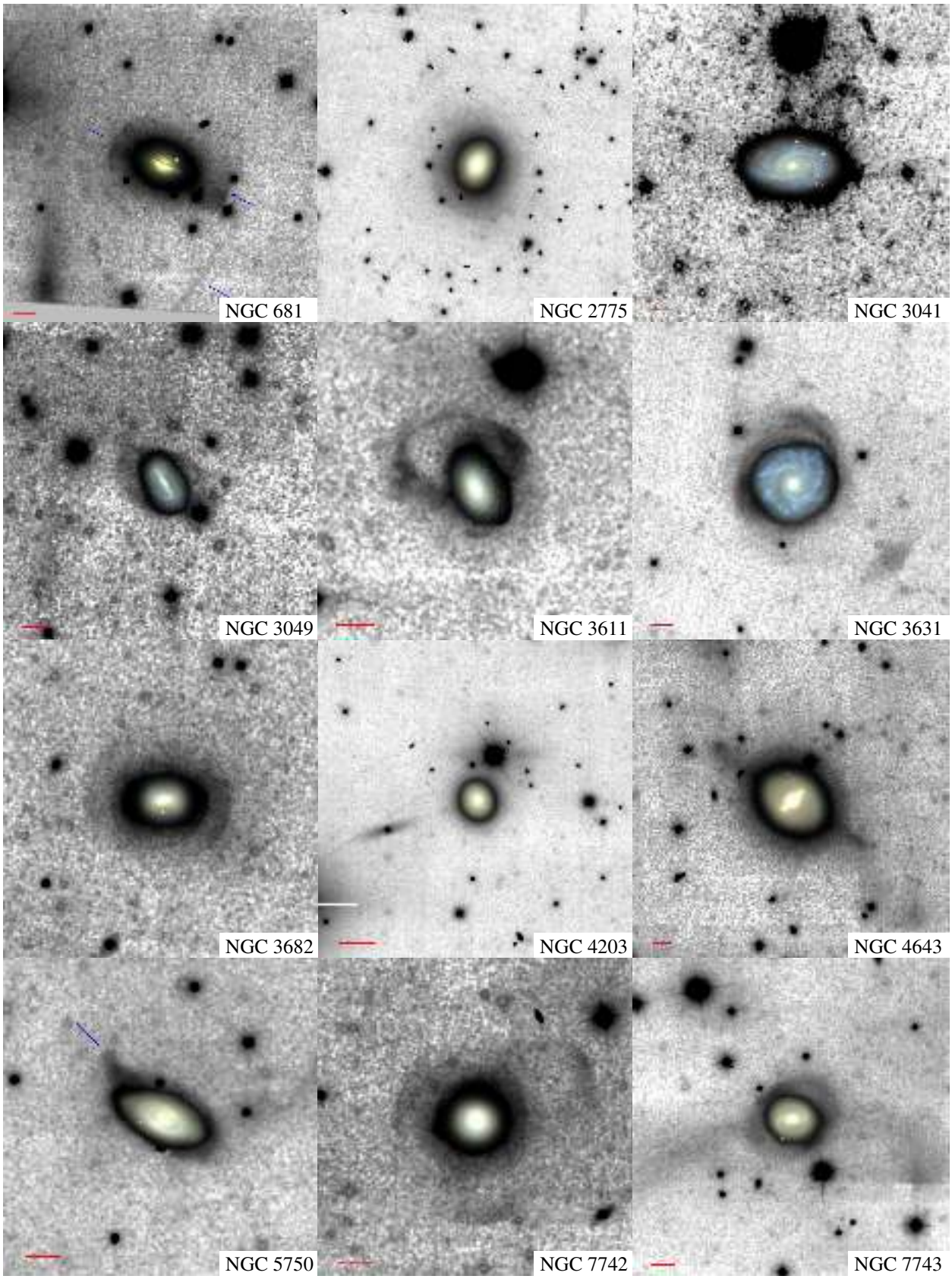

Fig. 8: Confirmed tidal streams from Table A.1 detected by stacking $g-r-i$ SDSS bands as described in this work. Streams already reported in previous publications are not included. The red lines indicate a scale of 3 arcminutes. In some cases, blue arrows indicate structures of interest described in Section 3.3. North is up and east to the left.

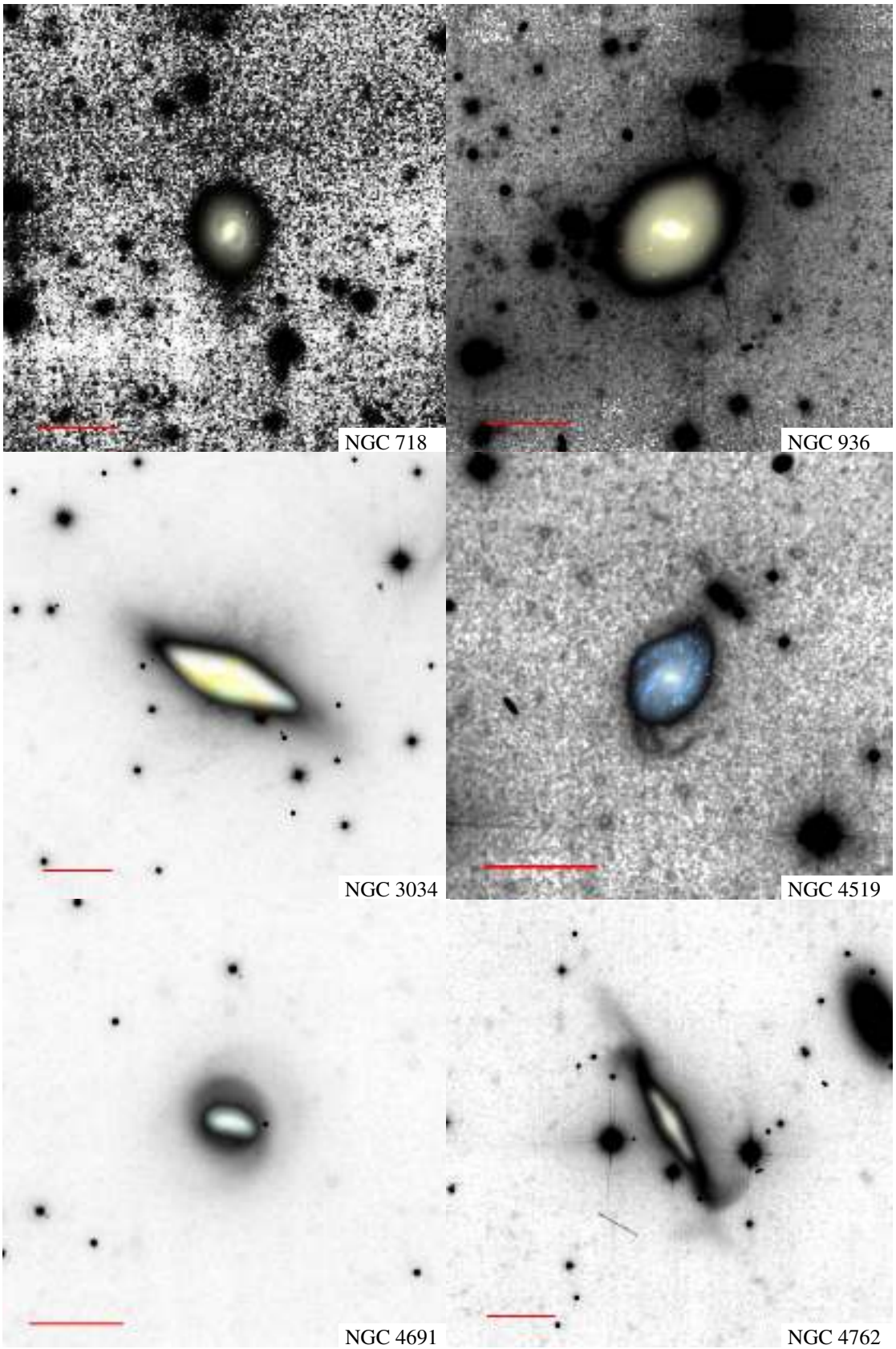

Fig. 9: Selection of the diffuse-light features detected around some of the galaxies listed in Table A.1. Deeper data are needed to confirm their origin (tidal streams, galactic perturbations, extended spiral arms, etc). The red lines indicate a scale of 3 arcminutes. North is up and east to the left.

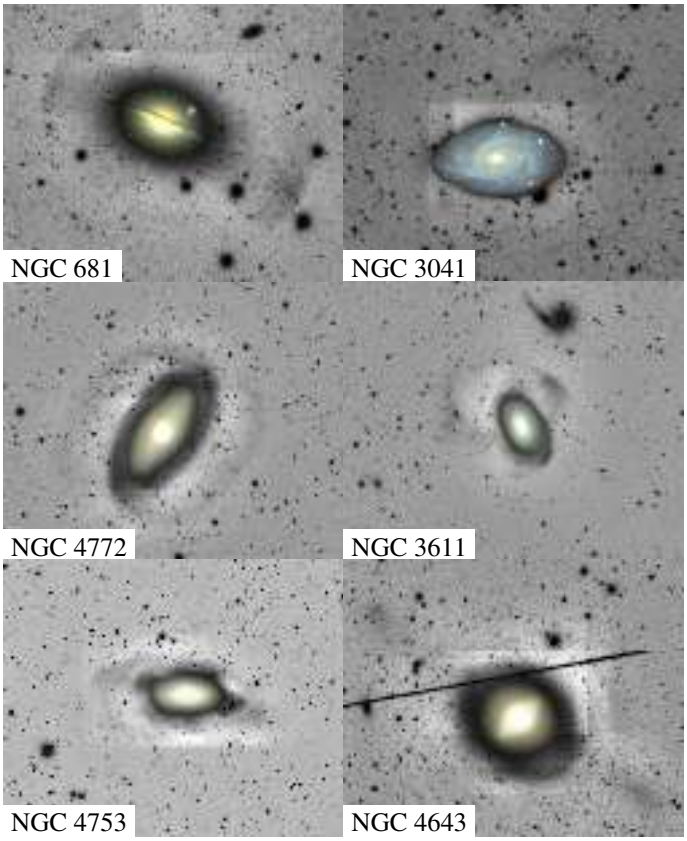

Fig. 10: Images taken from DECaLS public survey, confirming some of our findings. See Figure 8 for more information. A color inset of the disk of each galaxy taken from this survey has been included as reference.

4. Conclusions

We have estimated the frequency of stellar tidal streams in the halos of massive galaxies in the local Universe by processing SDSS images to reveal low surface brigthness features, using a technique similar to that of Miskolczi et al. (2011). Our results are summarized in Table A.1. To facilitate statistical comparisons with cosmological simulations of galaxy formation, we have defined a volume-, mass-, and size-limited parent sample of galaxies with stellar masses similar to that of the Milky Way based on the S^{4}G catalog. From the 2331 galaxies listed by S^{4}G, our sample selects 297 targets from the SDSS footprint (excluding low Galactic latitudes, major mergers, and the Virgo cluster). We estimate that the typical surface brightness limit of the SDSS images for these galaxies (after stacking their *g*, *r*, and *i* band images) is 28.1 $\pm$ 0.3 mag arcsec^{-2}.

By visual inspection, we detected a total of 28 confirmed tidal streams, including new features discovered in this study and some previously known tidal streams. Therefore, our most conservative estimate is that 9% of the galaxies in our sample show evidence of diffuse features that may be linked to minor merging events (either stellar or gaseous streams, or a mixture of both). This fraction of galaxies displaying tidal features does not include the possible new, but unconfirmed detections listed in Table A.1. When we also count the systems with high-confidence detections (i.e., with a DCL of 3 or 4), the frequency of tidal features in our sample rises to 14%. It is important to remark that some of these diffuse-light features may not be the signature of dwarf satellite remnants, but instead Galactic cirrus, imaging artifacts, or distorted spiral arms. This underscores the importance of deeper observations to confirm the nature of these features (see Fig. 4).

These results are broadly consistent with comparable studies cited in Section 1, in particular those listed in Table 1 from Atkinson et al. (2013). Although the surface brightness limits of the observations used in these earlier studies are more or less compatible, the wide variety of sample selections limits a more detailed comparison of the final results. Bright tidal features are expected to be relatively more likely in ETGs, while the only analogous study for disk galaxies (Miskolczi et al. 2011) was also less statistically representative of the galaxy population because it was focused on testing the image processing method. Comparisons with simulations are still needed, and will be reported elsewhere.

Last, because our procedure for enhancing images to detect low surface brightness features relies on stacking images in multiple filters and because those features have an intrinsically low S/N, we cannot measure their colours. To do so, deeper multiband imaging is needed, and will be valuable to constrain stellar populations and masses of the merging systems. Discussion of the physical properties of the features we detected and their comparison to the newest simulations is beyond the scope of this article. These topics will be addressed in a forthcoming paper.

Acknowledgements. GM thanks Arpad Miskolczi for the image processing training and the SDSS images showed in Fig. 6, and the Astronomisches Institut der Ruhr-Universitat Bochum for their hospitality during his visit. GM also thanks Gabriel Torrealba for his help in mapping the SDSS DR10 footprint, and Néstor Espinoza for his comments on the statistics of the sample. DMD thanks the team of astrophotographers from the STSS: Mark Hanson, Adam Block and Ken Crawford for their images shown in this work; Giuseppe Donatiello for his help with the presentation of some figures; and Seppo Laine for his help with the target selection and comments. APC acknowledges the support of STFC Grant ST/P000541/1. We also thank the anonymous referee for their constructive comments in the revision stage. The authors acknowledge the use of the Spitzer Survey of Stellar Structure in Galaxies and the Dark Energy Camera Legacy Survey as a core part of this work. The authors also acknowledge the use of IRAF, the Image Reduction and Analysis Facility, a general purpose software system for the reduction and analysis of astronomical data. IRAF is written and supported by the National Optical Astronomy Observatories (NOAO) in Tucson, Arizona. NOAO is operated by the Association of Universities for Research in Astronomy (AURA), Inc. under cooperative agreement with the National Science Foundation. Funding for SDSS-III has been provided by the Alfred P. Sloan Foundation, the Participating Institutions, the National Science Foundation, and the U.S. Department of Energy Office of Science. This work made use of the following Python 3 libraries: Matplotlib (Hunter 2007), SciPy (Jones et al. 2001–), NumPy. This research also made use of Astropy, a community-developed core Python package for Astronomy (Astropy Collaboration et al. 2013).

References

Abadi, M. G., Navarro, J. F., & Steinmetz, M. 2006, MNRAS, 365, 747
Abazajian, K. N., Adelman-McCarthy, J. K., Agüeros, M. A., et al. 2009, ApJS, 182, 543
Ahn, C. P., Alexandroff, R., Allende Prieto, C., et al. 2014, ApJS, 211, 17
Amorisco, N. C. 2017a, MNRAS, 464, 2882
Amorisco, N. C. 2017b, MNRAS, 469, L48
Astropy Collaboration, Robitaille, T. P., Tollerud, E. J., et al. 2013, A&A, 558, A33
Atkinson, A. M., Abraham, R. G., & Ferguson, A. M. N. 2013, ApJ, 765, 28
Bertin, E. & Arnouts, S. 1996, A&AS, 117, 393
Blanton, M. R., Kazin, E., Muna, D., Weaver, B. A., & Price-Whelan, A. 2011, AJ, 142, 31
Blum, R. D., Burleigh, K., Dey, A., et al. 2016, in American Astronomical Society Meeting Abstracts, Vol. 228, American Astronomical Society Meeting Abstracts, 317.01
Blumenthal, G. R., Faber, S. M., Primack, J. R., & Rees, M. J. 1984, Nature, 311, 517
Boselli, A., Cuillandre, J. C., Fossati, M., et al. 2016, A&A, 587, A68
Brodie, J. P., Romanowsky, A. J., Strader, J., et al. 2014, ApJ, 796, 52
Bullock, J. S. & Johnston, K. V. 2005, ApJ, 635, 931

Bullock, J. S., Kolatt, T. S., Sigad, Y., et al. 2001, MNRAS, 321, 559
Caldwell, J. A. R., McIntosh, D. H., Rix, H.-W., et al. 2008, ApJS, 174, 136
Chonis, T. S. & Gaskell, C. M. 2008, AJ, 135, 264
Chonis, T. S., Martínez-Delgado, D., Gabany, R. J., et al. 2011, AJ, 142, 166
Cole, S., Lacey, C. G., Baugh, C. M., & Frenk, C. S. 2000, MNRAS, 319, 168
Cooper, A. P., Cole, S., Frenk, C. S., et al. 2010, MNRAS, 406, 744
Cooper, A. P., D'Souza, R., Kauffmann, G., et al. 2013, MNRAS, 434, 3348
Crnojević, D., Sand, D. J., Spekkens, K., et al. 2016, ApJ, 823, 19
Croton, D. J., Springel, V., White, S. D. M., et al. 2006, MNRAS, 365, 11
Davis, M., Efstathiou, G., Frenk, C. S., & White, S. D. M. 1985, ApJ, 292, 371
de Blok, W. J. G., Józsa, G. I. G., Patterson, M., et al. 2014, A&A, 566, A80
De Lucia, G. & Helmi, A. 2008, MNRAS, 391, 14
D'Souza, R., Kauffman, G., Wang, J., & Vegetti, S. 2014, MNRAS, 443, 1433
Duc, P.-A., Cuillandre, J.-C., Karabal, E., et al. 2015, MNRAS, 446, 120
Duc, P.-A. & Renaud, F. 2013, in Lecture Notes in Physics, Berlin Springer Verlag, Vol. 861, Lecture Notes in Physics, Berlin Springer Verlag, ed. J. Souchay, S. Mathis, & T. Tokieda, 327
Eisenstein, D. J., Weinberg, D. H., Agol, E., et al. 2011, AJ, 142, 72
Fazio, G. G., Hora, J. L., Allen, L. E., et al. 2004, ApJS, 154, 10
Font, A. S., Johnston, K. V., Bullock, J. S., & Robertson, B. E. 2006, ApJ, 638, 585
Fritze, K., Lange, M., Moestl, G., Oleak, H., & Richter, G. M. 1977, Astronomische Nachrichten, 298, 189
Gunn, J. E., Carr, M., Rockosi, C., et al. 1998, AJ, 116, 3040
Gunn, J. E., Siegmund, W. A., Mannery, E. J., et al. 2006, AJ, 131, 2332
Guo, Q. & White, S. D. M. 2008, MNRAS, 384, 2
Hammer, F., Puech, M., Chemin, L., Flores, H., & Lehnert, M. D. 2007, ApJ, 662, 322
Harmsen, B., Monachesi, A., Bell, E. F., et al. 2017, MNRAS, 466, 1491
Haynes, M. P., Jore, K. P., Barrett, E. A., Broeils, A. H., & Murray, B. M. 2000, AJ, 120, 703
Hunter, J. D. 2007, Computing In Science & Engineering, 9, 90
Ibata, R. A., Lewis, G. F., McConnachie, A. W., et al. 2014, ApJ, 780, 128
Javanmardi, B., Martinez-Delgado, D., Kroupa, P., et al. 2016, A&A, 588, A89
Johnston, K. V., Bullock, J. S., Sharma, S., et al. 2008, ApJ, 689, 936
Johnston, K. V., Sackett, P. D., & Bullock, J. S. 2001, ApJ, 557, 137
Jones, E., Oliphant, T., Peterson, P., et al. 2001–, SciPy: Open source scientific tools for Python
Karachentsev, I. D. & Kashibadze, O. G. 2006, Astrophysics, 49, 3
Kauffmann, G., White, S. D. M., & Guiderdoni, B. 1993, MNRAS, 264, 201
Kaviraj, S. 2010, MNRAS, 406, 382
Lacey, C. & Cole, S. 1993, MNRAS, 262, 627
Laine, S., Knapen, J. H., Muñoz-Mateos, J.-C., et al. 2014, MNRAS, 444, 3015
Leaman, R., Erroz-Ferrer, S., Cisternas, M., & Knapen, J. H. 2015, MNRAS, 450, 2473
Ludwig, J., Pasquali, A., Grebel, E. K., & Gallagher, III, J. S. 2012, AJ, 144, 190
Malin, D. & Hadley, B. 1997, PASA, 14, 52
Martínez-Delgado, D., D'Onghia, E., Chonis, T. S., et al. 2015, AJ, 150, 116
Martínez-Delgado, D., Gabany, R. J., Crawford, K., et al. 2010, AJ, 140, 962
Martínez-Delgado, D., Peñarrubia, J., Gabany, R. J., et al. 2008, ApJ, 689, 184
Martínez-Delgado, D., Peñarrubia, J., Jurić, M., Alfaro, E. J., & Ivezić, Z. 2007, ApJ, 660, 1264
Martínez-Delgado, D., Pohlen, M., Gabany, R. J., et al. 2009, ApJ, 692, 955
Martínez-Delgado, D., Romanowsky, A. J., Gabany, R. J., et al. 2012, ApJ, 748, L24
McConnachie, A. W., Irwin, M. J., Ibata, R. A., et al. 2009, Nature, 461, 66
Merritt, A., van Dokkum, P., Danieli, S., et al. 2016, ApJ, 833, 168
Miskolczi, A., Bomans, D. J., & Dettmar, R.-J. 2011, A&A, 536, A66
Mouhcine, M. & Ibata, R. 2009, MNRAS, 399, 737
Muñoz, R. P., Puzia, T. H., Lançon, A., et al. 2014, ApJS, 210, 4
Muñoz-Mateos, J. C., Sheth, K., Regan, M., et al. 2015, ApJS, 219, 3
Okamoto, S., Arimoto, N., Ferguson, A. M. N., et al. 2015, ApJ, 809, L1
Pillepich, A., Madau, P., & Mayer, L. 2015, ApJ, 799, 184
Press, W. H. & Schechter, P. 1974, ApJ, 187, 425
Purcell, C. W., Bullock, J. S., & Zentner, A. R. 2007, ApJ, 666, 20
Querejeta, M., Meidt, S. E., Schinnerer, E., et al. 2015, ApJS, 219, 5
Rodriguez-Gomez, V., Pillepich, A., Sales, L. V., et al. 2016, MNRAS, 458, 2371
Schaye, J., Crain, R. A., Bower, R. G., et al. 2015, MNRAS, 446, 521
Schweizer, F. & Seitzer, P. 1990, PASP, 102, 615
Searle, L. & Zinn, R. 1978, ApJ, 225, 357
Sheth, K., Regan, M., Hinz, J. L., et al. 2010, PASP, 122, 1397
Spavone, M., Capaccioli, M., Napolitano, N. R., et al. 2017, A&A, 603, A38
Steiman-Cameron, T. Y., Kormendy, J., & Durisen, R. H. 1992, AJ, 104, 1339
Thomas, G. F., Famaey, B., Ibata, R., Lüghausen, F., & Kroupa, P. 2017, A&A, 603, A65
Trujillo, I., Martinez-Valpuesta, I., Martínez-Delgado, D., et al. 2009, ApJ, 704, 618
Vogelsberger, M., Genel, S., Springel, V., et al. 2014, MNRAS, 444, 1518
Wang, M.-Y., Fattahi, A., Cooper, A. P., et al. 2017, MNRAS, 468, 4887
Werner, M. W., Roellig, T. L., Low, F. J., et al. 2004, ApJS, 154, 1
White, S. D. M. & Rees, M. J. 1978, MNRAS, 183, 341
Whitmore, B. C., Lucas, R. A., McElroy, D. B., et al. 1990, AJ, 100, 1489
York, D. G., Adelman, J., Anderson, Jr., J. E., et al. 2000, AJ, 120, 1579
Zucker, D. B., Kniazev, A. Y., Bell, E. F., et al. 2004, ApJ, 612, L121

Appendix A: Supplementary tables.

ID	Galaxy morphology	Distance (Mpc)	log(Stellar Mass) ($M_\odot$)	DCL	Tags	Comments
NGC 681	SAB	33.600	10.752	4	S C	This work
NGC 718	SAB	21.400	10.283	3	C E	Very faint arc-like feature to the north plus possible overdensity to the south
NGC 936	SB0	20.683	10.926	3	C E	Double arc-like feature; hints of warped disk
NGC 1055	SBb	16.630	10.739	4	O	Martínez-Delgado et al. (2010)
NGC 1084	SAc	21.225	10.619	4	C	Martínez-Delgado et al. (2010)
NGC 2775	SAab	17.000	10.870	4	S	This work; MD+
NGC 2859	(R)SB0	27.333	10.882	3	C Sph	Two possible partially disrupted satellites within a ring, with leading and trailing tails
NGC 3034	I0	3.777	10.449	2	E O	Possible spike features
NGC 3041	SAB	26.350	10.437	4	C	This work
NGC 3049	SBab	30.775	10.132	4	S C E	This work; MD+
NGC 3185	(R)SBa	24.725	10.215	3	C E O	Very faint loop connected to the disk, with a compact object embedded on it
NGC 3277	SA	25.000	10.375	1	S	Possible shells very close to the halo
NGC 3521	SABbc	12.078	11.030	4	S C E O	Martínez-Delgado et al. (2010)
NGC 3611	SAa	33.300	10.462	4	C	Schweizer & Seitzer (1990); This work
NGC 3628	Sb	11.300	10.805	4	Sph	Martínez-Delgado et al. (2010)
NGC 3631	SAc	13.102	10.163	4	E O	This work; MD+
NGC 3675	SA	17.200	10.919	1	E	Candidate tidal overdensities, not clearly distinguishable from disk warping
NGC 3682	SA0	ND	10.230	4	S	This work
NGC 3729	SB	20.183	10.233	3	Sph E	Possible satellite being disrupted
NGC 3877	SA	15.612	10.445	1	E O	Asymmetrical and coplanar spike extending from the disk
NGC 3949	SA	18.341	10.246	3	S E	Possible shell very close to the outer disk
NGC 4013	Sb	18.600	10.630	4	E O	Martínez-Delgado et al. (2010)
NGC 4051	SAB	14.575	10.359	3	Sph E O	Possible compact object with halo and tail, plus an overdensity south of the galaxy
NGC 4111	SA0	15.550	10.452	4	Sph O	Brodie et al. (2014)
NGC 4203	SAB0	14.940	10.528	4	Sph	This work
NGC 4262	SB0	20.510	10.377	2	E	Two overdensities not clearly related to tidal features, perhaps part of the disk
NGC 4293	(R)SB0	14.320	10.418	3	E O	Clear substructure in the inner halo, very close to the disk
NGC 4394	(R)SB	16.800	10.440	3	E	Possible extended disk features, or tidal arcs surrounding the galaxy
NGC 4414	SAc	18.312	10.883	4	S	de Blok et al. (2014)
NGC 4494	E	13.841	10.542	2	O	Possible diffuse substructure, resembling symmetric spikes in an elliptical galaxy
NGC 4519	SB	28.411	10.191	3	C E	Filamentary feature with two components, likely related to either the halo or the disk
NGC 4569	SABab	12.352	10.638	4	E O	Martínez-Delgado et al. (2010)
NGC 4594	SAa	10.390	11.253	4	C	Malin & Hadley (1997)
NGC 4631	SBd	6.050	10.127	4	E O	Martínez-Delgado et al. (2015)
NGC 4643	SB0	25.700	11.028	4	C Sph	This work
NGC 4651	SAc	26.708	10.844	4	S C E O	Martínez-Delgado et al. (2010)
NGC 4691	(R)SB0	22.500	10.479	2	E O	Possible outer halo overdensity with the appearance of a dense stellar cloud
NGC 4753	I0	16.869	10.930	4	E	Steiman-Cameron et al. (1992)
NGC 4762	SB0	22.460	10.848	2	E O	An interesting case of disk warping with mixed tidal features
NGC 4772	SAa	30.475	10.747	4	E	Haynes et al. (2000)
NGC 4866	SA0	23.800	10.689	1	E O	Unclassifiable disk feature to the right of the galaxy, possibly with tidal origin
NGC 5055	SAbc	8.333	10.778	4	C O	Martínez-Delgado et al. (2010)
NGC 5364	SA	19.513	10.614	3	E O	Giant tidal structure west of the galaxy

Table A.1 continued from previous page

ID	Galaxy morphology	Distance (Mpc)	log(Stellar Mass) ($M_\odot$)	DCL	Tags	Comments
NGC 5506	S pec	23.833	10.122	3	C O	Distorted, asymmetric tidal features connected to each side of the disk
NGC 5576	E	23.930	10.770	1	S	Possible diffuse shells
NGC 5750	SB0	33.633	10.741	4	E O	This work
NGC 5806	SAB	25.541	10.585	3	C S E	Diffuse extended overdensity, with a shell or arc-like feature very close to the disk
NGC 5907	SAc	16.636	10.871	4	C	Martínez-Delgado et al. (2010)
NGC 7241	SB	ND	10.263	4	E O	Leaman et al. (2015)
NGC 7742	SAb	22.200	10.343	4	S C	This work
NGC 7743	(R)SB0	21.433	10.447	4	C E	This work; MD+

Table A.1: Tidal streams found in this work, including previously known features and new discoveries (28 host galaxies), with detection confidence levels (DCL) 3 and 4. Diffuse-light overdensities, with their physical nature yet to be confirmed (23 host galaxies) are also included, with DCL 1 and 2. This implies a total of 51 galaxies with any type of tidal features related to them. Distances and stellar masses were taken from S^4G, while their morphology was extracted from NED database. Additionally, substructures we found have been tagged: *S* for shells; *C* for curved, arcuated features, including anything coherent and stream like; *Sph* for spheroidal satellites and partially disrupted cores; *E* for extensions of the central galaxy (e.g. warps and spiral arms); and *O* for any other type of less common features (wedges, radial spikes, fuzzy clouds of debris, etc.). For known substructures, references of previous studies have been supplied. MD+ refers to Martínez-Delgado et al. (in prep.), a forthcoming paper.

NGC 7814	NGC 2967	NGC 3495	NGC 3992	NGC 4343	NGC 4904	NGC 5792
NGC 157	NGC 2964	NGC 3501	IC 749	NGC 4356	NGC 5005	NGC 5821
NGC 337	UGC 5228	NGC 3507	IC 750	NGC 4369	NGC 5033	NGC 5854
NGC 584	NGC 3003	NGC 3512	NGC 4030	NGC 4380	NGC 5112	NGC 5864
NGC 615	NGC 3021	NGC 3556	NGC 4045	IC 3322A	NGC 5145	NGC 5879
NGC 628	NGC 3044	NGC 3596	NGC 4062	UGC 7522	NGC 5205	NGC 5921
NGC 660	NGC 3055	NGC 3623	NGC 4085	NGC 4405	IC 902	NGC 5963
NGC 676	NGC 3031	NGC 3626	NGC 4088	NGC 4448	UGC 8614	NGC 5956
NGC 693	NGC 3067	NGC 3629	NGC 4096	NGC 4451	NGC 5248	NGC 5957
NGC 701	NGC 3098	NGC 3637	NGC 4100	NGC 4461	NGC 5301	NGC 5962
NGC 779	NGC 3162	NGC 3642	NGC 4102	NGC 4503	NGC 5300	NGC 5964
IC 210	NGC 3177	NGC 3655	NGC 4123	NGC 4437	NGC 5334	NGC 5970
NGC 864	NGC 3185	NGC 3666	NGC 4138	NGC 4527	NGC 5356	NGC 6015
NGC 955	NGC 3184	NGC 3669	NGC 4145	NGC 4536	NGC 5422	NGC 6012
NGC 1022	NGC 3198	NGC 3681	NGC 4157	NGC 4559	NGC 5443	IC 1158
NGC 1035	IC 610	NGC 3684	UGC 7267	NGC 4565	NGC 5457	NGC 6106
UGC 4551	NGC 3254	NGC 3683	NGC 4212	NGC 4580	NGC 5473	NGC 6217
NGC 2654	NGC 3259	NGC 3686	NGC 4217	NGC 4599	NGC 5480	NGC 7280
NGC 2683	NGC 3279	NGC 3692	NGC 4220	NGC 4632	NGC 5520	NGC 7497
NGC 2712	NGC 3294	NGC 3755	NGC 4237	NGC 4639	NGC 5507	NGC 7625
NGC 2742	NGC 3346	NGC 3756	NGC 4260	NGC 4666	NGC 5584	NGC 1052
NGC 2770	NGC 3351	IC 719	NGC 4274	NGC 4710	NGC 5668	NGC 2768
NGC 2780	NGC 3359	NGC 3810	UGC 7387	NGC 4746	NGC 5690	NGC 3193
NGC 2805	NGC 3370	NGC 3900	NGC 4303	NGC 4771	NGC 5713	NGC 3608
NGC 2820	NGC 3389	NGC 3898	NGC 4307	NGC 4800	IC 1048	NGC 4278
NGC 2844	NGC 3430	NGC 3938	NGC 4314	NGC 4808	NGC 5746	NGC 5173
NGC 2841	NGC 3437	NGC 3953	NGC 4316	NGC 4826	NGC 5768	NGC 5216
NGC 2903	NGC 3486	NGC 3982	NGC 4324	NGC 4845	NGC 5798	NGC 5846

Table A.2: Galaxies with no evidence of observable diffuse overdensities in our sample of 297 galaxies.

Draft version April 6, 2018
Preprint typeset using LaTeX style emulateapj v. 12/16/11

DISCOVERY OF A VAST IONIZED GAS CLOUD IN THE M51 SYSTEM

Aaron E. Watkins[1,2], J. Christopher Mihos[2], Matthew Bershady[3], Paul Harding[2]

Draft version April 6, 2018

ABSTRACT

We present the discovery of a vast cloud of ionized gas 13′ (32 kpc) north of the interacting system M51. We detected this cloud via deep narrow-band imaging with the Burrell Schmidt Telescope, where it appears as an extended, diffuse Hα-emitting feature with no embedded compact regions. The Cloud spans ∼10′×3′ (25×7.5 kpc) in size and has no stellar counterpart; comparisons with our previous deep broadband imaging show no detected continuum light to a limit of $\mu_{\rm lim,B}$ ∼30 mag arcsec^{-2}. WIYN[a] SparsePak observations confirm the cloud's kinematic association with M51, and the high [N II]/Hα, [S II]/Hα, and [O I]/Hα line ratios we measure imply a hard ionization source such as AGN photoionization or shock heating rather than photoionization due to young stars. Given the strong [N II] emission, we infer roughly solar metallicity for the cloud, ruling out an origin due to infall of primordial gas. Instead we favor models where the gas has been expelled from the inner regions of the M51 system due to tidal stripping or starburst/AGN winds and has been subsequently ionized either by shocks or a fading AGN. This latter scenario raises the intriguing possibility that M51 may be the nearest example of an AGN fossil nebula or light echo, akin to the famous "Hanny's Voorwerp" in the IC 2497 system.

Keywords: galaxies: individual(M51), galaxies: interactions, galaxies: jets, galaxies: intergalactic medium, ISM: jets and outflows

1. INTRODUCTION

The galaxy pair M51 (NGC 5194/5) is perhaps the most iconic interacting system. It has been a subject of study since the 1800s, its spiral structure serving as a key element in early debates over the true nature of galaxies (Steinicke 2012). It has served, via simulations and observations, as an important dynamical benchmark for studies of tidal tails (e.g., Toomre & Toomre 1972; Burkhead 1978; Rots et al. 1990; Salo & Laurikainen 2000) and spiral density waves (e.g., Dobbs et al. 2010). Because of its active star formation (star formation rate (SFR) ∼ 1.6 $M_\odot$ yr^{-1}; Kennicutt et al. 2009) and close distance (8.6 Mpc; McQuinn et al. 2016), it is also often used to calibrate star formation tracers and gas density–SFR relations (e.g., Calzetti et al. 2005; Kennicutt et al. 2007). Yet despite this scrutiny, the system continues to yield surprises.

For example, while M51 is known to host extended gaseous tidal debris (Rots et al. 1990), the detailed impact of the interaction and subsequent star formation and nuclear activity on this extended gas is poorly understood. Narrow-band imaging by Hoopes et al. (2001) also shows an anomalous "hook" of ionized gas overlapping the companion galaxy, possibly stripped from the primary and shock-heated during the interaction. However, while M51 has been the frequent target of narrow-band imaging and spectroscopy (e.g., Hoopes et al. 2001; Thilker et al. 2002; Calzetti et al. 2005; Kennicutt et al. 2007), to date these have lacked the wide field coverage necessary to explore the pair's extreme outskirts where more extended and diffuse ionized gas could reside.

In this Letter, we present the discovery of a new such feature in M51: a large, diffuse circumgalactic cloud of ionized gas (hereafter, the Cloud), spanning ∼10′×3′ (25×7.5 kpc) in size and located ∼13′ (32 kpc) north of NGC 5194's center. We discovered this Cloud through deep wide-field narrow-band imaging using the Burrell Schmidt Telescope at Kitt Peak National Observatory (KPNO). We present the results of this imaging, as well as follow-up spectroscopy done with the Sparsepak Integral Field Unit (IFU) at the WIYN 3.5m Telescope (Bershady et al. 2004, 2005). We discuss the Cloud's possible origins given its properties and our current understanding of the M51 system.

2. OBSERVATIONS AND DATA REDUCTION

2.1. *Narrow-band imaging*

We observed M51 with the Burrell Schmidt in the Spring of 2015 using two custom ∼100 Å-wide narrowband filters designed to target Hα+[N II] emission and the adjacent continuum in nearby (D< 20 Mpc) galaxies. We observed M51 only on moonless, photometric nights in March, April, and May. The Schmidt field of view covers 1.°65×1.°65; in each filter we imaged M51 in 77×1200s images, randomly dithering pointings by ∼30′ around the target. We also observed 33 offset night sky fields alongside ∼100 twilight exposures to build flat fields (described further below; however, for details, see Watkins et al. 2017). Finally, we targeted a variety of spectrophotometric standard stars from Massey et al. (1988) for flux calibration.

We began data reduction with standard bias subtraction and nonlinearity corrections. For flat-fielding, we used a combination of night sky and twilight sky images. Due to the low count rate in the narrow-band night sky images, we combined the twilight sky images to build preliminary flat fields. However, because of the Burrell Schmidt's large field of view, these flats contain strong gradients induced by the twilight sky; we thus used the night-sky flats to model and remove these linear gradients (Watkins et al. 2017). To remove mild (<1% amplitude) fringing from the on-band exposures, we isolated the fringe pattern from the combined on-band night-

[1] Astronomy Research Unit, University of Oulu, FIN-90014, Finland
[2] Department of Astronomy, Case Western Reserve University, Cleveland, OH 44106, USA
[3] Department of Astronomy, University of Wisconsin, 475 N. Charter Street, Madison, WI 53706, USA
[a] The WIYN Observatory is a joint facility of the University of Wisconsin-Madison, Indiana University, the National Optical Astronomy Observatory and the University of Missouri.

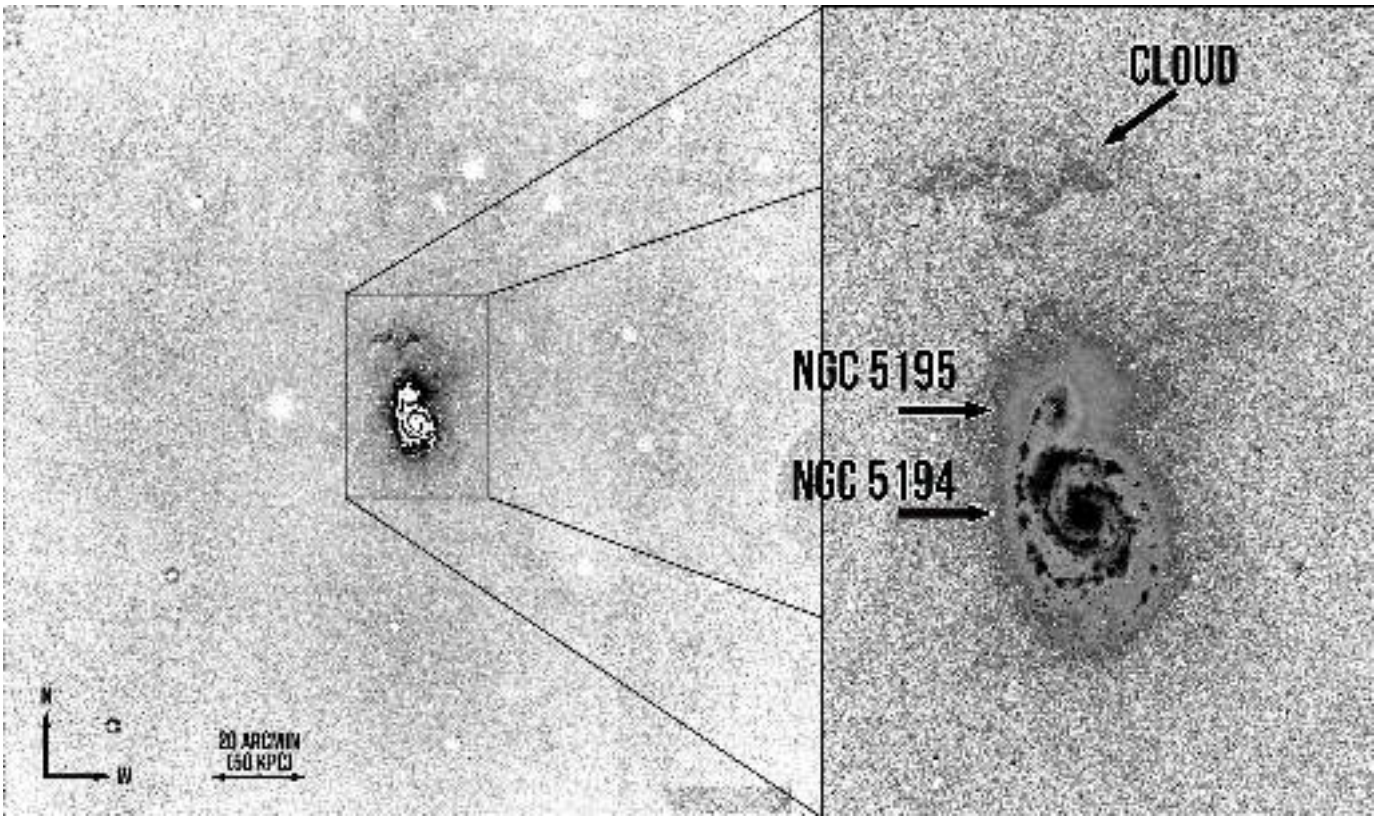

Figure 1. Left: Hα difference mosaic (see text), masked of bright sources and 3×3 pixel median-binned to emphasize diffuse Hα emission in M51 and the surrounding environment. The image has a per-pixel RMS noise of 5.7×10^{-19}ergs s^{-1} cm^{-2} arcsec^{-2}; the faintest emission visible is at $\sim10^{-18}$ ergs s^{-1} cm^{-2} arcsec^{-2}. **Right:** a zoomed-in view, showing the unbinned Hα difference mosaic at high dynamic range.

sky flats through division by the on-band twilight flat (where the fringe pattern was not visible against the much brighter flat field), then scaled and subtracted a normalized version of this fringe map from each frame using IRAF's[4] RMFRINGE package.

To reduce the effects of scattered light, we used long (1200s) exposures of Arcturus to model and remove internal reflections and the extended wings of the PSF from bright ($V \lesssim$10 mag) stars in each frame (see Slater et al. 2009). For each frame, we then hand-masked all stars, galaxies, and any scattered light artifacts, modeled the remaining sky as a plane, and subtracted it. Finally, we median combined the images to create three final image stacks with total exposure times of 25.6 hr: an on-band mosaic (composed of all on-band exposures), an off-band mosaic (similarly defined), and a "difference" mosaic created by combining individual difference images between on-off pairs observed sequentially in time (Figure 1). We use the difference images to illustrate the morphology of the diffuse Hα, but conduct quantitative photometry on the on- and off-band mosaics directly.

2.2. *Sparsepak spectroscopy*

We obtained follow-up spectroscopy of the Cloud in April 2017 using Sparsepak (Bershady et al. 2004, 2005). Sparsepak, comprised of 82 4.687″ diameter fibers, feeds into the WIYN Bench Spectrograph. We centered Sparsepak on the region with the brightest emission, where the 72″ × 72″coverage spans the far western end of the Cloud (Figure 2). To target Hα emission, we used the 860 line mm^{-1} grating in 2$^{\rm nd}$ order, to cover 6187Å to 7096Å at a resolution of $\lambda/\delta\lambda$ = 3380 (σ ∼37 km s^{-1}). We fully resolve Hα, [N II] 6548/6583Å, and [S II] 6716/6731Å from each target.

We took 1200s exposures of the target, chopping to a nearby sky field on occasion to yield more accurate sky subtraction. Our final object spectrum contains 31 target exposures, with 23 accompanying sky exposures of the same length. We used the IRAF tasks IMCOMBINE and CCDPROC for basic image processing (bias, overscan and dark subtraction, and cosmic ray removal) and DOHYDRA for spectral extraction, channel-to-channel correction (via accompanying dome flat exposures), and wavelength calibration (via accompanying ThAr arc lamp exposures). Calibration data were taken over the course of the run.

Due to the target's low surface brightness, we subtract sky independently of DOHYDRA, augmenting the method described in Appendix D of (Bershady et al. 2005) to take advantage of independent sky exposures. Briefly, we first we fit low-order polynomials in wavelength to each extracted fiber aperture in the combined sky frames, rejecting sky-lines via clipping, to produce a sky flat. The flat is normalized and applied to both combined object and sky extracted spectra. The sky spectra are then subtracted from the object spectra, fiber by fiber; this yields excellent subtraction of the sky continuum but leaves residuals in the sky-lines due to different line-to-line temporal variations. To remove these sky-line residuals we fit low-order polynomials, with clipping, in the pseudo-slit dimension for each wavelength channel. The resulting reduced spectrum is shown in 3, coadded from the seven fibers

[4] IRAF is distributed by the National Optical Astronomy Observatory, which is operated by the Association of Universities for Research in Astronomy (AURA) , Inc., under cooperative agreement with the National Science Foundation.

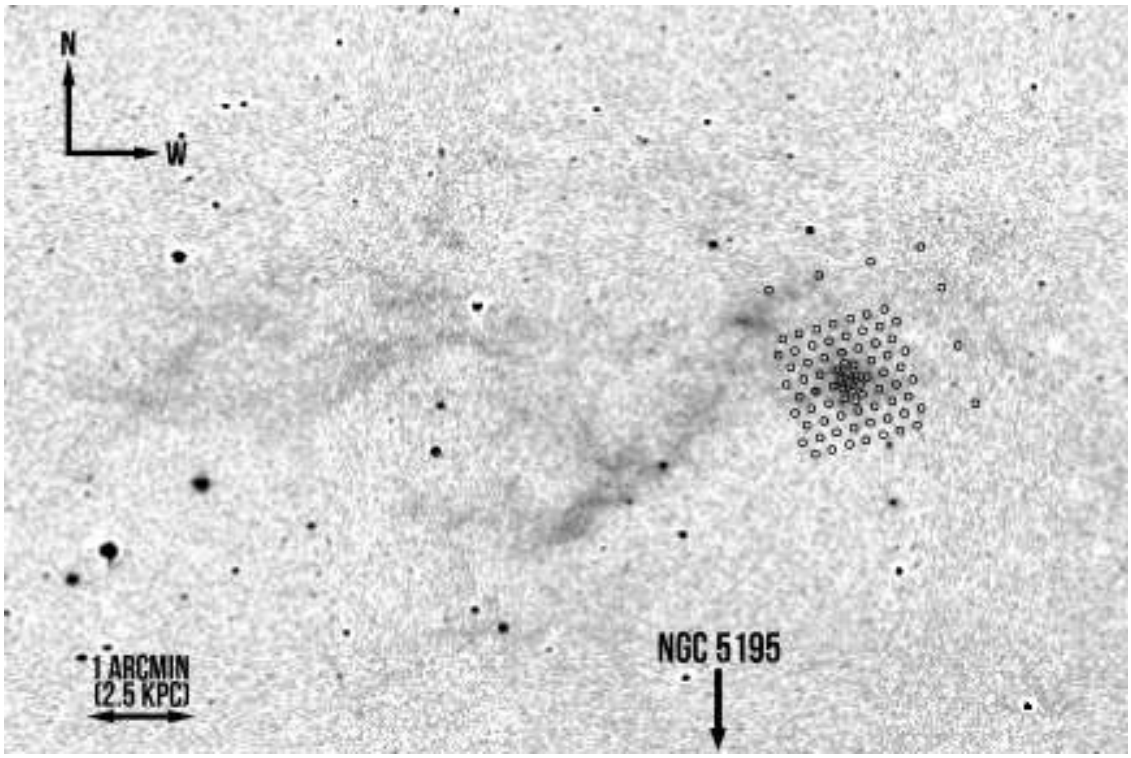

Figure 2. Close-up of the Cloud in the Hα difference image, with the Sparsepak fiber array orientation overlaid.

Table 1
Cloud Properties

$(\alpha, \delta)_{\rm peak}$	13h29m51.1s, +47d24m34s
Dimensions	10′×3′ (25×7.5 kpc)
$f_{H\alpha,tot}$	1.8×10^{-13} ergs s^{-1} cm^{-2}
$L_{H\alpha,tot}$	1.6×10^{39} erg s^{-1}
Peak $\Sigma_{H\alpha}$	2.2×10^{-16} ergs s^{-1} cm^{-2} arcsec^{-2}
$V_{heliocentric}$	637 ± 13 km s^{-1}
log([N II]6748,6583 / Hα)	+0.17
log([N II]6583 / Hα)	+0.06
log([S II]6717,6731 / Hα)	−0.10
log([S II]6717 / [S II]6731)	+0.14
log([O I]6300 / Hα)	−0.77
log([O III]5007 / Hα)	< −0.64

with the strongest [N II]λ6583Å signal. The sky spectrum is shown for comparison; note that at this Cloud's velocity, all five targeted lines strongly overlap with telluric line emission.

3. RESULTS

We provide the Cloud's basic properties in Table 1, while Figure 1 shows the Cloud's morphology and position relative to M51. It is expansive (∼25 kpc long), and though it is near M51 on the sky, aside from some very faint ($\Sigma_{H\alpha} \lesssim 1.6 \times 10^{-18}$ ergs s^{-1} cm^{-2} arcsec^{-2}) diffuse emission northwest of the companion it shows no clear connection to the system. From polygonal aperture photometry (e.g., Watkins et al. 2015) of the narrow-band imaging, we measure the Cloud's total Hα+[N II] luminosity as $\sim4 \times10^{39}$ ergs s^{-1}. From the co-added Sparsepak spectra, the Cloud's mean [N II] (6583+6548)/Hα ratio is ∼1.48, hence the Cloud's total Hα luminosity is $L_{H\alpha}\sim1.6\times10^{39}$ ergs s^{-1}.

We detect this Hα emission, the [N II] and [S II] doublets, and faint [O I]λ6300Å in seven of the Sparsepak fibers; Hα and [N II]λ6583Å are visible in an additional 17 fibers. Doing a combined fit to the [N II], [S II], and Hα lines for the seven fibers with the brightest [N II] emission, we measure a heliocentric velocity of 637 ± 13 km s^{-1}; the quoted uncertainty is the standard deviation of the individual fiber measurements, most of which is astrophysical variance in radial velocity. This velocity is well outside the realm of most Milky Way emission, including high velocity clouds (HVCs), which typically have velocities < 500 km s^{-1} (and none of which have been discovered so near M51 on the sky; Westmeier 2018). The Cloud's observed velocity is within the range of H I velocities observed in the M51 system (Rots et al. 1990), confirming its kinematic association with the interacting pair.

In the left panel of Figure 4, we overlay contours of Hα emission (convolved with a 3×3 pixel Gaussian kernel to emphasize diffuse features) on a deep Burrell Schmidt *B*-band image of M51 (Watkins et al. 2015). The cloud appears to have no stellar counterpart; it is undetected in the broadband imaging to a limit of μ_B ∼30 mags arcsec^{-2}, nor is it detected in our similarly deep Washington *M* image (Watkins et al. 2015). The three apertures with spectral continuum in Figure 3 each have line-emission consistent with background galaxies. Its non-detection in Washington *M* also implies a low [O III]λ5007Å flux: $< 5 \times 10^{-17}$ ergs s^{-1} cm^{-2} arcsec^{-2}, or log([O III]/Hα) < −0.64. The Cloud lies just east of M51's diffuse northwestern stellar plume, and shows morphological contiguity with the northernmost of the bifurcated western streams extending from the companion, whose faintest extension arcs toward it. We also note a marginal detection of diffuse far ultraviolet emission near the Cloud (Bigiel et al. 2010), however it is coincident with 12 μm emission visible in the *WISE* Galactic cirrus map (Meisner & Finkbeiner 2014) of the region, and hence cannot be firmly associated with the Cloud.

The right panel of Figure 4 shows H I contours from the

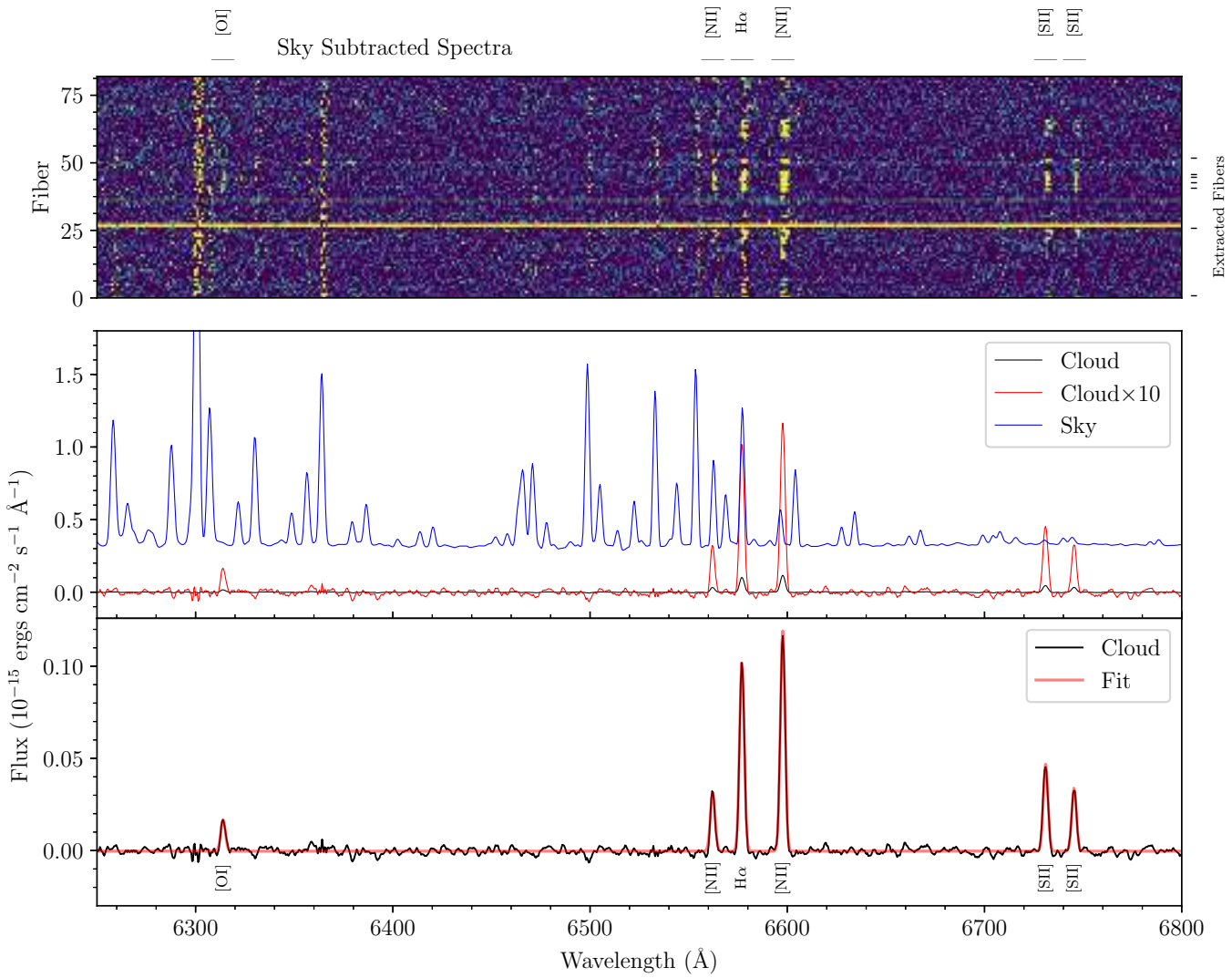

Figure 3. Top: final reduced extracted 2D spectrum of the Cloud. The seven fibers used in co-addition are marked on the right. **Middle:** final reduced co-added spectrum of the Cloud. The reduced spectrum is shown in black; the red curve scales this spectrum's intensity up by ×10 to show weak emission lines. The foreground sky spectrum (blue) is shown to illustrate the strong overlap between the Cloud's redshifted emission lines and telluric lines. **Bottom:** fitted spectrum (red) overlaid on the Cloud's reduced spectrum (black).

interferometry map of Rots et al. (1990) overlaid on our Hα difference mosaic. While no high column density H I (>3.3×10^{19} cm^{-2}) lies directly coincident with the Cloud, diffuse H I potentially associated with it is found throughout the region (Pisano, private communication). We measure a ∼ 40 km s^{-1} gradient across the central fiber bundle, oriented northeast to southwest (with the highest velocities in the east); this orientation is similar to velocity gradients across the two high velocity (520–660 km s^{-1}; Rots et al. 1990) H I clouds straddling it, implying a potential connection as well.

The [N II], [S II], and [O I] lines give additional information on the Cloud's ionization source. From the co-added spectrum (Figure 3), we measure log([N II]λ6584/Hα) = +0.06, log([S II]$\lambda\lambda$6716,31/Hα) = −0.10, and log([O I]λ6300/Hα) = −0.77. Variations in the sky subtraction model yield line ratio uncertainties of < 0.1 dex, similar to fiber-to-fiber differences between individual fiber spectra across the field. These line ratios are significantly higher than those in H II regions, and are more typical of hard photoionization from AGN (e.g., Kewley et al. 2006). In AGN-ionized clouds, the [N II]/Hα line ratio is largely a metallicity indicator (e.g., Fu & Stockton 2009) over a wide range of ionization parameters, and in the case of the M51 Cloud, suggests roughly solar metallicity for the gas.

Alternatively, the gas may be shocked. From MAPPINGS III (Allen et al. 2008) shock models, the Cloud's [N II]/Hα, [S II]/Hα, and [O I]/Hα line ratios are well-matched by shock velocities between ∼200–300 km s^{-1}. In these shock models as well, [N II]/Hα favors solar metallicity or higher.

In summary, the Cloud's relatively high velocity rules out a chance projection of foreground Milky Way gas, and demonstrates the Cloud's kinematic association with tidally stripped H I gas in the M51 system. The lack of broadband light and the high [N II]/Hα, [S II]/Hα, and [O I]/Hα line ratios argue against ionization from young stars and instead suggest ionization from AGNs or shocks. With the Cloud's association with M51 now well-established, in the next section we explore possible scenarios to explain the Cloud's origin and anomalous line ratios.

4. DISCUSSION

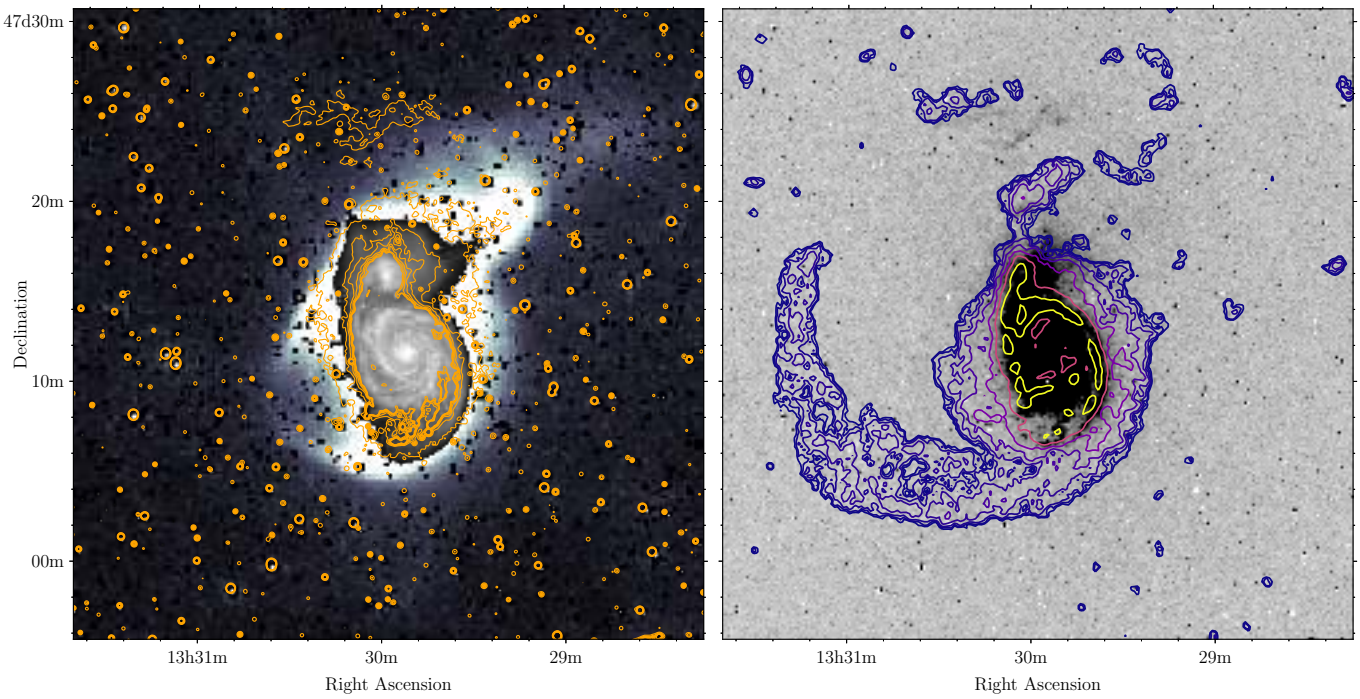

Figure 4. Left: Hα-emission contours (orange) overlaid on a deep B-band image of M51 from Watkins et al. (2015). The inner regions of M51 have been rescaled in intensity to show its high surface brightness structure. **Right:** H I contours from the 34″ resolution VLA interferometry map of Rots et al. (1990) overlaid on our Hα difference mosaic.

While the Cloud's physical association with M51 is well-demonstrated, its origin is less clear. M51 is dynamically complex, with active star formation (Kennicutt et al. 2009), numerous and disorganized tidal features (Rots et al. 1990; Watkins et al. 2015), and nuclear activity in both galaxies (Ho et al. 1997; Rampadarath et al. 2018). In such a system, a number of plausible scenarios are available to explain the Cloud's origin, including tidal or ram-pressure stripping during the interaction, infall from the surrounding circumgalactic environment, or ejection from a central starburst or AGN. Constraints on the metallicity and excitation mechanism at work in the Cloud can help differentiate between these various possibilities.

The roughly solar metallicity indicated by the [N II]/Hα line ratio constrains the gas' provenance. Such a high metallicity argues against scenarios that involve gas infalling from the circumgalactic environment, which should have lower metallicities (∼1/3 solar; Prochaska et al. 2017). Instead, the Cloud likely comes from M51's similarly high metallicity inner regions (Bresolin et al. 2004). This in turn supports models where the Cloud is tidally stripped gas or, alternatively, gas ejected from M51 via winds from AGN or starburst activity. Strong outflows of gas are seen in many starburst galaxies (e.g., Dahlem et al. 1998) and AGN (e.g., Feruglio et al. 2010), reaching large distances from the host galaxy.

Given M51's ongoing interaction, tidal stripping is perhaps the most obvious origin for the Cloud. This scenario is supported by the Cloud's kinematic contiguity with M51's observed tidal H I, as well as the morphological connection between the Cloud and the NE hook at the end of NGC 5195's western tidal tail. Further information comes from existing numerical simulations which explore M51's interaction history (e.g., Hernquist 1990; Salo & Laurikainen 2000; Durrell et al. 2003). The Cloud's far northern location and high relative velocity provide the tightest constraints on the models — only the multi-passage model of Salo & Laurikainen (2000) reproduces any such gas. In this model, this gas is first elevated above NGC 5194's disk plane in response to the companion's initial passage, then is pulled downward along the line of sight by the second encounter. If this model is correct, the Cloud could represent gas initially stripped out and then met by the companion at high velocity during the second passage, resulting in shock-heating (Dopita & Sutherland 2003). From MAPPINGS III models (Allen et al. 2008), shock velocities between ∼200–300 km s^{-1} reproduce the Cloud's observed line ratios, in good agreement with the 174 ± 13 km s^{-1} line of sight velocity difference between the Cloud and NGC 5194. However, turbulence in shocked gas should also broaden the lines, yet we measure typical line FWHM of only ∼60 km s^{-1}. This particular model for the M51 system also must necessarily be incomplete as it (and all other simulations to date) fails to reproduce all of the system's extended tidal features (Watkins et al. 2015).

While the Cloud may be tidally stripped, appealing to shock heating as its ionization source may also suffer from a timescale problem. Following Fossati et al. (2016), we can estimate the Cloud's recombination timescale from its density; using an updated derivation of the [S II] density estimator Sanders et al. (2016), the Cloud's log([S II]λ6716/6731) ratio of 0.14 yields $n \sim 50$ cm^{-3}, for a recombination time of ∼2000 yr, orders of magnitude shorter than the estimated time of last passage (50–500 Myr, e.g., Howard & Byrd 1990; Salo & Laurikainen 2000; Durrell et al. 2003). However, these constraints may not be so severe. First, the uncertainty on the [S II] line ratio encompasses the low density limit of the [S II] density estimator, allowing for significantly lower densities and longer recombination times. Second, recently Gavazzi et al. (2017) argued that a diffuse cloud of ionized gas in the Coma Cluster could be as old as 85 Myr. Similarly, a network of shock-excited Hα-emitting filaments is seen extend-

ing ∼120 kpc between the galaxies M86 and NGC 4438 in the Virgo Cluster (Kenney et al. 2008); the time since closest approach between these two galaxies is thought to be ∼100 Myr ago. These observations suggest that some mechanism can prolong the lifespans of such clouds well beyond the recombination timescale. In galaxy clusters like Coma or Virgo, this mechanism is likely ongoing ram-pressure effects from the hot intracluster medium. While M51 is not in a cluster environment, numerical simulations suggest that strong galaxy interactions can lead to the formation of hot halo gas (Sinha & Holley-Bockelmann 2009) and may provide a similar mechanism here.

Alternatively, the high line ratios observed in the Cloud could be due to hard photoionization from either a central AGN or starburst driven winds. "Hanny's Voorwerp", a circumgalactic cloud near the fading AGN IC 2497 (Keel et al. 2012) provides a comparable example of the former; in IC 2497, it is believed that a recent interaction triggered a central AGN which illuminated and ionized the Voorwerp before nuclear activity ceased $\sim 10^5$ years ago (evidenced by a radio jet pointing toward the Voorwerp; Keel et al. 2012). A similar scenario may be playing out in M51, where both galaxies host active nuclei (Ho et al. 1997; Rampadarath et al. 2018) and weak nuclear jets (though only NGC 5195's jet is currently aligned with the Cloud; Ford et al. 1985; Rampadarath et al. 2018), although the lack of strong [O III] emission implied by our broadband imaging suggests the Cloud could be older than the Voorwerp (Binette & Robinson 1987). The currently weak nuclear activity in M51 provides another similarity with the IC 2497 system; following the method employed by Lintott et al. (2009) we find that the current nuclear X-ray luminosity of either galaxy is too faint by four orders of magnitude to account for the Cloud's total $L_{H\alpha}$, implying that if the Cloud were ionized by AGN emission, the AGN has since faded significantly. This does not rule out past AGN activity, however, as the strength of such activity, and the jet angle, can evolve on <1 Myr timescales (Denney et al. 2014; Nawaz et al. 2016).

Finally, the Cloud may be the result of starburst driven "superwinds" (Heckman et al. 1990), in which outflows from young massive stars and supernovae in a galaxy's disk generate expanding bubbles of hot gas through the IGM. These bubbles can "blow out" and generate localized shocks in density inhomogeneities in the galaxy's gaseous halo tens to hundreds of kiloparsecs from the starburst (Heckman et al. 1990, 2017). One nearby example is the "cap" of ionized gas observed ∼10 kpc north of the starburst galaxy M82 (Devine & Bally 1999; Lehnert et al. 1999), which lies parallel to M82's disk and in direct line with its starburst winds (clearly outlined in Hα and X-ray emission; Lehnert et al. 1999). However, M51 contains no known features indicative of superwinds, its SFR is a factor of two lower than that in M82 (after correcting for extinction; Lehnert et al. 1999; Kennicutt et al. 2009), and the Cloud is much more distant from M51 than the cap is from M82 (>32 kpc, i.e., the projected distance). If the shock front is traveling at 300 km s^{-1} (as we estimate from MAPPINGS III models; Allen et al. 2008), this implies the proposed superwind shock front has been propagating for >100 Myr, significantly longer than starburst durations in most known superwind galaxies (typically of order 10^7 yr; Heckman et al. 1990). Therefore, this scenario appears unlikely unless the Cloud's orientation with respect to NGC 5194's disk was significantly more favorable in the past.

5. SUMMARY

We report the discovery of a vast, diffuse ionized gas cloud projected 13′ (32 kpc) north of the interacting galaxy pair M51. The Cloud spans 13′×3′ (25×7.5 kpc) in size, and its systemic velocity (637 ± 13 km s^{-1}) confirms its association with the M51 system. The Cloud has no embedded star formation, and its high [N II]/Hα, [S II]/Hα, and [O I]/Hα line ratios suggest AGN photoionization or shock heating. While not directly overlapping with M51's tidal features, the Cloud shows mild evidence of morphological contiguity with the companion galaxy's bifurcated western arm, and kinematic similarity to adjacent tidally stripped H I.

The strong [N II] emission implies high solar-like metallicities, such that rather than being primordial infall, the Cloud has likely been expelled from the inner disk of NGC 5194 via tidal stripping or AGN/starburst winds. The currently low level of nuclear activity in both galaxies implies that if the Cloud were ionized by AGN activity, this activity has since faded (a situation similar to IC 2497 and Hanny's Voorwerp; Lintott et al. 2009; Keel et al. 2012). Alternatively, the Cloud may have been ejected by starburst driven "superwinds" (Heckman et al. 1990), however M51's low SFR relative to known superwind galaxies (e.g., M82; Devine & Bally 1999; Lehnert et al. 1999), as well as the Cloud's extreme distance from M51 (>32 kpc), suggests that this scenario is less likely. Finally, the gas may be shock heated due to the ongoing interaction between the galaxy pair; if so, it may lend support to the multi-passage interaction model of M51 proposed by Salo & Laurikainen (2000), to date the only such model to produce significant high velocity gas north of the system.

To discriminate between these various scenarios for the Cloud's origin, additional spectroscopic observations are needed which target emission lines that probe the Cloud's density and temperature structure, better constrain its metallicity, and differentiate between photoionization and shock-heating models for the Cloud. Additional information would come from mapping the line ratios and kinematics of the Cloud across its spatial extent as well.

The Cloud's size and structure — and, perhaps most importantly, the proximity of the M51 system — provide a unique opportunity to study the detailed effects of feedback and ionization on the circumgalactic environments of galaxies. The local universe contains very few known examples of extended diffuse emission sources like the Cloud; each new example provides a wealth of new information about tidal interactions, feedback processes, and the mutual interaction between galaxies and their environment. In particular, if the Cloud is a fossil nebula or echo of strong AGN activity in M51, it would be the most nearby example of a rapidly fading AGN, and also represent a new and critical piece to our understanding of the iconic M51 system.

We thank Heikki Salo and Eija Laurikainen for useful discussions regarding dynamical models of M51, and Tim Heckman, Bill Keel, and the anonymous referee for useful suggestions. Support for this project was provided by NSF/AST-1108964 (JCM) and NSF/AST-1517006 (MAB).

Facilities: CWRU:Schmidt, WIYN

REFERENCES

Allen, M. G., Groves, B. A., Dopita, M. A., Sutherland, R. S., & Kewley, L. J. 2008, ApJS, 178, 20-55
Bershady, M. A., Andersen, D. R., Harker, J., Ramsey, L. W., & Verheijen, M. A. W. 2004, PASP, 116, 565
Bershady, M. A., Andersen, D. R., Verheijen, M. A. W., et al. 2005, ApJS, 156, 311
Bigiel, F., Leroy, A., Walter, F., et al. 2010, AJ, 140, 1194
Binette, L., & Robinson, A. 1987, A&A, 177, 11
Bresolin, F., Garnett, D. R., & Kennicutt, R. C., Jr. 2004, ApJ, 615, 228
Burkhead, M. S. 1978, ApJS, 38, 147
Calzetti, D., Kennicutt, R. C., Jr., Bianchi, L., et al. 2005, ApJ, 633, 871
Dahlem, M., Weaver, K. A., & Heckman, T. M. 1998, ApJS, 118, 401
Denney, K. D., De Rosa, G., Croxall, K., et al. 2014, ApJ, 796, 134
Devine, D., & Bally, J. 1999, ApJ, 510, 197
Dobbs, C. L., Theis, C., Pringle, J. E., & Bate, M. R. 2010, MNRAS, 403, 625
Dopita, M. A., & Sutherland, R. S. 2003, Astrophysics of the diffuse universe, (Berlin, New York: Springer)
Durrell, P. R., Mihos, J. C., Feldmeier, J. J., Jacoby, G. H., & Ciardullo, R. 2003, ApJ, 582, 170
Feruglio, C., Maiolino, R., Piconcelli, E., et al. 2010, A&A, 518, L155
Ford, H. C., Crane, P. C., Jacoby, G. H., Lawrie, D. G., & van der Hulst, J. M. 1985, ApJ, 293, 132
Fossati, M., Fumagalli, M., Boselli, A., et al. 2016, MNRAS, 455, 2028
Fraternali, F., Marasco, A., Armillotta, L., & Marinacci, F. 2015, MNRAS, 447, L70
Fu, H., & Stockton, A. 2009, ApJ, 690, 953
Gavazzi, G., Consolandi, G., Yagi, M., & Yoshida, M. 2017, A&A, 606, A131
Heckman, T. M., Armus, L., & Miley, G. K. 1990, ApJS, 74, 833
Heckman, T. M., Borthakur, S., Wild, V., Schiminovich, D., & Bordoloi, R. 2017, ApJ, 846, 151
Hernquist, L. 1990, in Dynamics and Interactions of Galaxies, ed. R. Wielen (Berlin: Springer), 108
Ho, L. C., Filippenko, A. V., & Sargent, W. L. W. 1997, ApJS, 112, 315
Hoopes, C. G., Walterbos, R. A. M., & Bothun, G. D. 2001, ApJ, 559, 878
Howard, S., & Byrd, G. G. 1990, AJ, 99, 1798
Keel, W. C., Lintott, C. J., Schawinski, K., et al. 2012, AJ, 144, 66
Kenney, J. D. P., Tal, T., Crowl, H. H., Feldmeier, J., & Jacoby, G. H. 2008, ApJ, 687, L69
Kennicutt, R. C., Jr., Calzetti, D., Walter, F., et al. 2007, ApJ, 671, 333
Kennicutt, R. C., Jr., Hao, C.-N., Calzetti, D., et al. 2009, ApJ, 703, 1672-1695
Kewley, L. J., Groves, B., Kauffmann, G., & Heckman, T. 2006, MNRAS, 372, 961
Lehnert, M. D., Heckman, T. M., & Weaver, K. A. 1999, ApJ, 523, 575
Lintott, C. J., Schawinski, K., Keel, W., et al. 2009, MNRAS, 399, 129
Massey, P., Strobel, K., Barnes, J. V., & Anderson, E. 1988, ApJ, 328, 315
McQuinn, K. B. W., Skillman, E. D., Dolphin, A. E., Berg, D., & Kennicutt, R. 2016, ApJ, 826, 21
Meisner, A. M., & Finkbeiner, D. P. 2014, ApJ, 781, 5
Nawaz, M. A., Bicknell, G. V., Wagner, A. Y., Sutherland, R. S., & McNamara, B. R. 2016, MNRAS, 458, 802
Prochaska, J. X., Werk, J. K., Worseck, G., et al. 2017, ApJ, 837, 169
Rampadarath, H., Soria, R., Urquhart, R., et al. 2018, arXiv:1802.04417
Rots, A. H., Bosma, A., van der Hulst, J. M., Athanassoula, E., & Crane, P. C. 1990, AJ, 100, 387
Salo, H., & Laurikainen, E. 2000, MNRAS, 319, 377
Sanders, R. L., Shapley, A. E., Kriek, M., et al. 2016, ApJ, 816, 23
Sinha, M., & Holley-Bockelmann, K. 2009, MNRAS, 397, 190
Slater, C. T., Harding, P., & Mihos, J. C. 2009, PASP, 121, 1267
Steinicke, W. 2012, Journal of Astronomical History and Heritage, 15, 19
Thilker, D. A., Walterbos, R. A. M., Braun, R., & Hoopes, C. G. 2002, AJ, 124, 3118
Toomre, A., & Toomre, J. 1972, ApJ, 178, 623
Watkins, A. E., Mihos, J. C., & Harding, P. 2015, ApJ, 800, L3
Watkins, A. E., Mihos, J. C., & Harding, P. 2017, ApJ, 851, 51
Westmeier, T. 2018, MNRAS, 474, 289

Astronomy & Astrophysics manuscript no. discmet
April 10, 2018

Disk stars in the Milky Way detected beyond 25 kpc from its center

M. López-Corredoira[1,2], C. Allende Prieto[1,2], F. Garzón[1,2], H. Wang[3,4], C. Liu[3,4], L. Deng[3,4]

[1] Instituto de Astrofísica de Canarias, E-38205 La Laguna, Tenerife, Spain
[2] Departamento de Astrofísica, Universidad de La Laguna, E-38206 La Laguna, Tenerife, Spain
[3] Key Laboratory of Optical Astronomy, National Astronomical Observatories, Chinese Academy of Sciences, Beijing 100012, China
[4] University of Chinese Academy of Sciences, Beijing, 100012, China

Received xxxx; accepted xxxx

ABSTRACT

Context. The maximum size of the Galactic stellar disk is not yet known. Some studies have suggested an abrupt drop-off of the stellar density of the disk at Galactocentric distances $R \gtrsim 15$ kpc, which means that in practice no disk stars or only very few of them should be found beyond this limit. However, stars in the Milky Way plane are detected at larger distances. In addition to the halo component, star counts have placed the end of the disk beyond 20 kpc, although this has not been spectroscopically confirmed so far.
Aims. Here, we aim to spectroscopically confirm the presence of the disk stars up to much larger distances.
Methods. With data from the LAMOST and SDSS-APOGEE spectroscopic surveys, we statistically derived the maximum distance at which the metallicity distribution of stars in the Galactic plane is distinct from that of the halo populations.
Results. Our analysis reveals the presence of disk stars at $R > 26$ kpc (99.7% C.L.) and even at $R > 31$ kpc (95.4% C.L.).

Key words. Galaxy: structure – Galaxy: disk – Galaxy: abundances

1. Introduction

The disk of our Galaxy has an exponential radial profile (de Vaucouleurs & Pence 1978; Bahcall & Soneira 1980), which means that the density of stars quickly decreases away from the center, although in principle a few stars should be present at very large distances from the center and some of them could be detected. With a typical scale length of 2 kpc (López-Corredoira & Molgó 2014; hereafter LM14) and a solar neighborhood surface density of visible stars (main-sequence and giants) of 27 $M_\odot pc^{-2}$ (McKee et al. 2015), the surface density at a Galactocentric distance of $R = 25$ kpc would be $\sim 5{\times}10^3$ $M_\odot kpc^{-2}$. Only 2% of the mass is due to giant stars (McKee et al. 2015), which are bright enough to be detected spectroscopically at these distances, so that the mass density associated with the giants would be ~ 100 $M_\odot kpc^{-2}$, that is, only very few giant stars, but a significant number are expected to be detected.

Some authors (Freudenreich et al. 1994; Ruphy et al. 1996; Porcel et al. 1997; Sale et al. 2010; Minniti et al. 2011; Amôres et al. 2017) have argued that the density of disk stars at $R > 13-16$ kpc is dramatically reduced with respect to an extrapolation of the exponential disk with the scale length of the inner disk. However, it is suspected that they expected a significant drop-off of stars because the flare of the Galactic disk becomes strong at these Galactocentric distances (LM14), and the stars are therefore distributed over a much wider range of heights, which produces this apparent depletion of in-plane stars. The surface density may not fall off abruptly, but the stars would simply be redistributed at greater heights from the plane. The flare has also been confirmed kinematically with the measured thickening of the vertical velocity distribution (Wang et al. 2017).

Momany et al. (2006) and Reylé et al. (2009) investigated the outer disk, but limited to $R < 20$ kpc and with large uncertainties beyond 15 kpc. Carraro et al. (2010) found some young stars between 15 and 20 kpc from the Galactic center. Feast et al. (2014) speculated about the interpretation of five Cepheids in the outer disk 1-2 kpc from the plane, but their results are puzzling since the very young population (~ 100 Myr) of Cepheids typical of a spiral arm should not be as farther away from $z = 0$ plane. Liu et al. (2017) reported that the disk seems to extend at least up to $R = 19$ kpc, and that beyond this radius the disk smoothly transitions to the halo without any truncation, break, or upward bending. These are further indications that the disk may not end at least out to $R = 20$ kpc, but what happens beyond this distance? Can we provide proof of the existence of disk stars farther away? The purpose of this paper is precisely answering this question. Certainly, there are stars beyond $R = 20$ kpc, but many of them belong to the old population of the halo (Xu et al. 2017). LM14 previously showed the existence of stars out to $R = 30$ kpc, although only in regions far from the plane, and without a spectroscopic classification of their age or metallicity.

2. Method

Our method in this paper is to search for a population typical of the thin disk, with a distribution of metallicities distinct from that of the halo, shifted toward higher metallicities. The halo metallicity distribution function (MDF) peaks at around [Fe/H]=-1.6 (Beers & Christlieb 2005; Allende Prieto et al. 2014), while the MDF of the disk reaches its maximum between roughly -0.7 and +0.25, depending upon the height over the midplane and the radial distance. (Hayden et al. 2015). Hence, metallicity by itself is useful to separate between halo and disk populations.

Specifically, our method consists of comparing the distribution of metallicities in two samples that satisfy i) a Galactocentric distance between R_1 and $R_1 + \Delta R$, $|z| < 5$ kpc and ii) a Galactocentric distance between R_2 and $R_2 + \Delta R$, $|z| \geq 5$ kpc. The reason we chose a height of $z = 5$ kpc for the separation of the two subsamples is that the scale height of the thick disk is approximately 1 kpc and the flare of the outer disk can

reach a thickness of several kpc for the disk (LM14). We set a fixed value of R_1 and ΔR and fit the value of R_2 in order to obtain the same average spherical Galactocentric distance for both distributions: $\langle r_1 \rangle \approx \langle r_2 \rangle$. This avoids the possible variation of the metallicity due to a gradient in the halo ([Fe/H] slightly depends on the spherical Galactocentric distance r; using data fom Fernández-Alvar et al. (2015, Fig. 6b), we derive a mean $\frac{d[Fe/H]}{dr} = -0.0121 \pm 0.0013$ kpc^{-1}). The non-sphericity of the halo is negligible at large radii (Xu et al. 2017).

Comparing distributions of heliocentric radial velocities might be another way of distinguishing halo and disk populations, but this is not so straightforward and would need a priori kinematic models to separate the contribution of different Galactocentric velocity components. We therefore do not use it here.

3. Data

We carried out our analysis with data on K-giants from LAMOST-DR3 (Liu et al. 2017) in the optical and SDSS-APOGEE-DR14 (Majewski et al. 2017) in the near-infrared.

The LAMOST DR3 catalog contains 5 756 075 spectra, for which the LAMOST pipeline has provided the metallicity [Fe/H], and the distances were estimated from a Bayesian approach (Carlin et al. 2015) with uncertainties of about 20%. About 70 000 K-giants were selected from LAMOST DR3 according to the criterion of Liu et al. (2014).

The Apache Point Galactic Evolution Experiment (APOGEE) DR14 (Abolfathi et al. 2017) includes millions of spectra for approximately 263,000 stars. Distances for the stars have been estimated with four different methods (Schultheis et al. 2014; Santiago et al. 2016; Wang et al. 2016; Holtzman et al. 2018) and were included in a value-added catalog released in conjunction with DR14. The agreement among the four codes is fair, typically within 20%. We have adopted for our analysis the average values of the available estimates, as well as the overall metallicity [M/H] values derived by the APOGEE ASPCAP pipeline (García Pérez et al. 2016), which for DR14 have been calibrated to match optical iron abundances ([Fe/H]) for clusters in the literature.

The spatial distribution of the stars considered here spans a range of Galactic longitudes that is accessible from observatories in the northern hemisphere, with those at larger R toward the anticenter. Although the overdensity of stars at $R \approx 20$ kpc was attributed by some authors to tidal debris of a dwarf galaxy (Monoceros Ring), LM14 have shown that this hypothesis is unnecessary and that the overdensity can be explained by a flared disk. Here we follow the argument of LM14.

4. Results

The metallicity distributions for different R_1 and for both surveys are given in Figs. 1 and 2. Possible selection effects on completeness do not affect the metallicity distribution (Nandakumar et al. 2017). A similar histogram was produced in Fig. 11 of Carlin et al. (2015) with LAMOST, but only with $R < 20$ kpc in the plane, whereas here we analyze the distributions beyond that limit. The metallicity of LAMOST halo stars was also analyzed (Xu et al. 2017), but without the stars in the plane with [Fe/H]> -1 that we include here. Tables 1 and 2 give the parameters of these distributions. The disk metallicity distribution peaks between -1.0 and -0.5, whereas the halo mean metallicity is a wider distribution with a maximum at about -1.5. The first range is expected

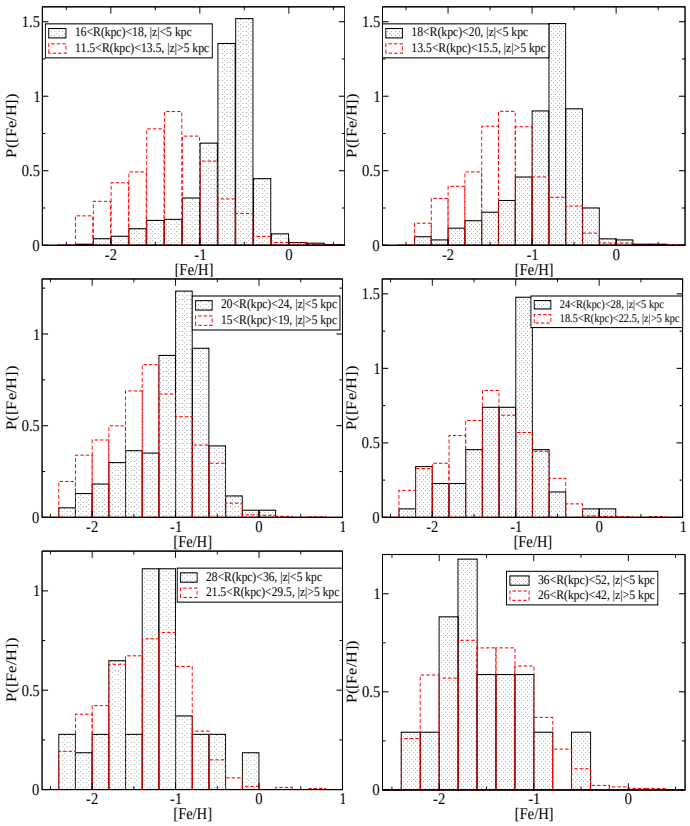

Fig. 1. Metallicity distributions [Fe/H] for different subsamples of LAMOST-DR3 K giants with $R_1 < R < R_1 + \Delta R$, $|z| < 5$ kpc, and $R_2 < R < R_2 + \Delta R$, $|z| \geq 5$ kpc, respectively, such that $\langle r_1 \rangle \approx \langle r_2 \rangle$. Normalized such that $\int d[Fe/H]P([Fe/H]) = 1$.

Table 1. Parameters in the comparison of metallicity distributions [Fe/H] for different subsamples of LAMOST-DR3 giants with $R_1 < R < R_1 + \Delta R$, $|z| < 5$ kpc, and $R_2 < R < R_2 + \Delta R$, $|z| \geq 5$ kpc, respectively, such that $\langle r_1 \rangle \approx \langle r_2 \rangle$. The first three columms indicate the Galactocentric radial range, columns 4 and 5 give the number of stars, column 6 gives the average signal-to-noise ratio of the first subsample, column 7 gives the average error of the [Fe/H] measurement in the first subsample, and column 8 gives the probability derived from a Kolmogorov-Smirnov test that the two metallicity distributions are identical within the random fluctuations. The distances are listed in kpc.

R_1	ΔR	R_2	N_1	N_2	$\langle S/N \rangle_1$	$\langle \Delta \mathrm{met} \rangle_1$	P_{K-S}
16	2	11.5	2160	1850	18.8	0.23	1.9E-298
18	2	13.5	699	1352	17.3	0.25	1.0E-99
20	4	15.0	359	1813	15.5	0.25	1.6E-27
24	4	18.5	88	992	14.2	0.26	0.014
28	8	21.5	54	936	12.6	0.24	> 0.32
36	16	26.0	17	649	11.0	0.28	> 0.32

from an extrapolation of the metallicity gradient from the inner disk, including both thin and thick disks (Besançon model simulation in López-Corredoira et al. 2007, Fig. 3).

The results are quite clear: significant differences are found for $R < 24$ kpc between the distributions in-plane and off-plane. The in-plane subsamples have disk and halo stars, whereas the

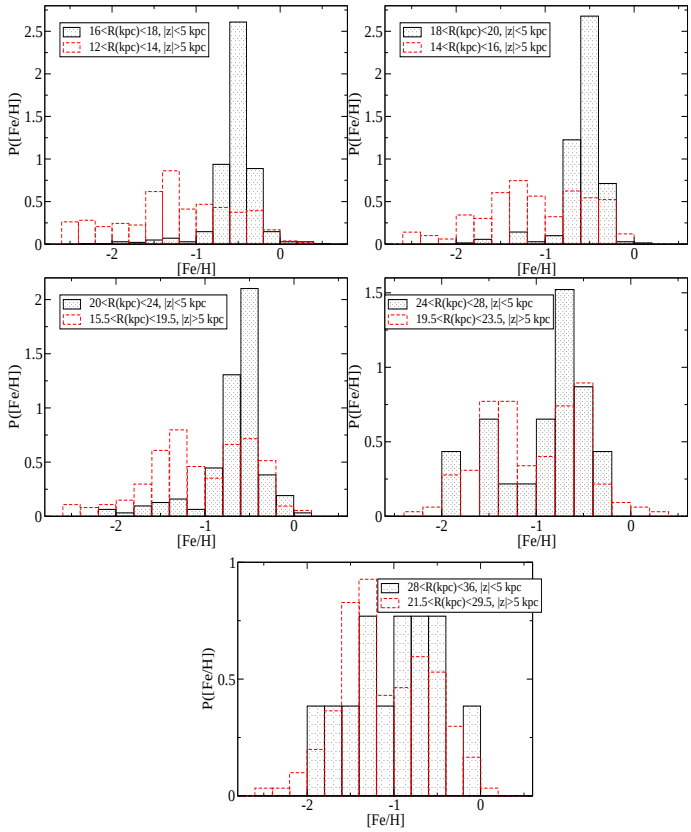

Fig. 2. Same as Fig. 1 for SDSS-APOGEE-DR14 stars.

Table 2. Same as Table 1 for SDSS-APOGEE-DR14 stars.

R_1	ΔR	R_2	N_1	N_2	$\langle S/N\rangle_1$	$\langle\Delta$met$\rangle_1$	P_{K-S}
16	2	12.0	715	267	180.2	0.03	4.0E-82
18	2	14.0	351	248	165.9	0.03	6.9E-38
20	4	15.5	157	370	148.7	0.03	1.1E-17
24	4	19.5	23	162	169.8	0.04	2.0E-3
28	8	21.5	13	151	123.0	0.04	> 0.32
36	16	–	0	–	–	–	–

off-plane subsample is composed of halo stars alone. No differences are found for $R > 28$ kpc in the plots.

The significance of the distributions was evaluated with a Kolmogorov-Smirnov (K-S) test, which is non-parametric and distribution independent. The K-S test has some limitations (Feigelson & Babu 2012), for instance, if the model that is compared with a data set was derived from the same data set, or when two distributions derived from data are not totally independent, but this is not the case here. Tables 1 and 2 give the probability assigned by this test to explain the different distributions as due to random fluctuations. Errors in [Fe/H] will decrease the K-S maximum distance $D_{\max}$ between the two distributions, thus increasing the probability P_{K-S}, so they cannot be responsible for a significant detection. When we vary R_1 and ΔR (in a range between 0.2 and 15.0 kpc) as free parameters, the maximum significance expressed in the equivalent number of sigmas for a given probability (assuming a normal distribution; i.e., 1σ is $P_{K-S} = 0.317$, 2σ is $P_{K-S} = 0.0455$, 3σ is $P_{K-S} = 2.70 \times 10^{-3}$, etc.) is given in Fig. 3. We can account for the effect of having a higher significance due to exploration of the values of R_1 if we fit a smooth function to the inferred significances, as done in Fig. 3. A cubic polynomial fitting (lower order polynomials do not yield a good fit) of the significance, results in a difference with halo stars at 99.73% C.L. (3σ) at $R_1 = 24.4$ kpc (LAMOST), $R_1 = 22.9$ kpc (APOGEE). A 5σ detection is found at $R_1 = 22.5$ kpc (LAMOST), $R_1 = 21.6$ kpc (APOGEE). A tentative detection at 2 σ is for $R_1 = 26.3$ kpc (LAMOST), $R_1 = 30.3$ kpc (APOGEE).

Both surveys independently yield the same results. The APOGEE data show a metallicity distribution for the disk that is narrower than in the LAMOST data, possibly due to the lower errors in the distance determination. The APOGEE spectra have a higher resolution and signal-to-noise ratio than the LAMOST observations, but a smaller spectral range. The off-plane stars in APOGEE present a double peak, whereas in LAMOST it has only one peak, possibly due to some miscalculation of disk stars for a great distance. The minimum detected metallicity in LAMOST is also limited at [Fe/H]=-2.5 (Carlin et al. 2015), but this difference in the histograms is not important because very few stars have metallicities lower than this limit. The remaining features in the distributions are equivalent.

The two surveys are independent because they have only very few sources in common: of 3393 sources in the LAMOST sample with $R > 16$ kpc, $|z| < 5$ kpc, only 96 were observed by APOGEE, which is a coincidence lower than 3%. These 96 stars have similar distance estimates and metallicities, which corroborates the reliability of their determinations. In addition, the surveys operate at different wavelengths, with different instruments and analysis pipelines. Therefore, we can combine the statistics of the two surveys as if they were independent: summing quadratically the number of sigmas of both surveys. This is also shown in Fig. 3. This global analysis of the two surveys shows that the significant detection of a difference in metallicity distribution in in-plane stars with respect to pure halo stars, interpreted as the presence of disk stars added to the halo sources, is given for $R > 23.2$ kpc at 5σ, $R > 26.0$ kpc at 3σ, and $R > 31.5$ kpc at 2σ.

For LAMOST, stars with $\langle R\rangle = 26.0$ kpc (3σ global detection) or $\langle R\rangle = 31.5$ kpc (2σ global detection) have a mean heliocentric distance of 18.3 kpc and 23.9 kpc, respectively; according to the analysis of Carlin et al. (2015, Fig. 2/right), in comparison with the Besançon model, the corresponding average systematic overestimation of distance is +2.2 and +3.2 kpc, respectively. Wang et al. (2017, appendix) claimed that the errors of the distances given by Carlin et al. (2015) are overestimated by a factor of two. Nonetheless, this excess of 1-3 kpc mainly affects stars with very low metallicity stars because the authors used isochrones with solar [α/Fe] (Carlin et al. 2015) and this should not affect the disk stars we analyzed at $|z| < 5$ kpc to find a distinction with halo population. The limit of the detection of disk stars should therefore not be significantly affected. For APOGEE, the distances were determined as the average of four independent methods that were compatible with each other within the errors (see §3), and the systematic error of heliocentric distances in comparison with cluster distances is underestimated by 4% (Wang et al. 2016). This is an average underestimation of -0.7 and -1.0 kpc for $\langle R\rangle = 26.0$ kpc (3σ global detection) or $\langle R\rangle = 31.5$ kpc, respectively, which places the stars even slightly farther away.

In order to further determine possible systematic errors, we excluded from our sample of APOGEE the stars with ASPCAP pipeline (García Pérez et al. 2016) flags (ASPCAPFLAG), which is a warning of some possible difficulties for an analysis of the star. This reduces the sample by 16% of sources (22 in-plane stars at $R > 24$ kpc instead of 37 without the cut),

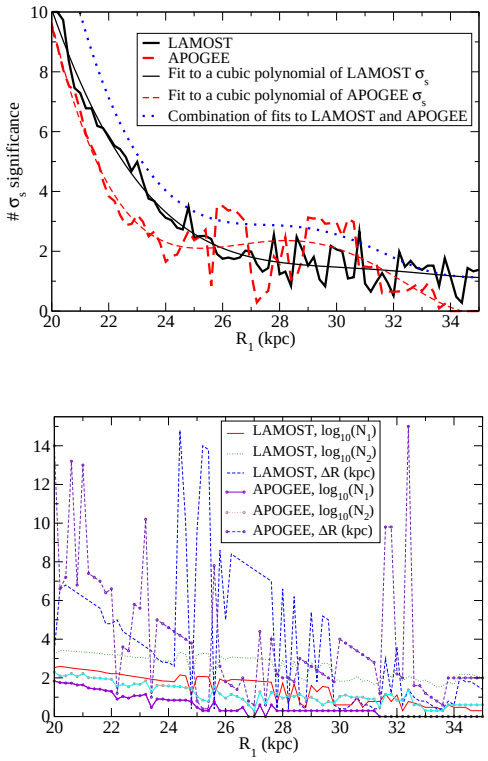

Fig. 3. Top: Maximum number (choosing the value of ΔR that gives the maximum value) of sigmas of significance detection of different metallicity distributions in the subsamples with $R > R_1$, $|z| < 5$ kpc, and $R > R_2$, $|z| \geq 5$ kpc, respectively, such that $\langle r_1 \rangle \approx \langle r_2 \rangle$. Bottom: Parameters N_1, N_2, and ΔR corresponding to that detection.

and the radius at which there is a 3σ detection is $R = 22.5$ kpc (instead of $R = 22.9$ kpc). If we furthermore add another constraint and also remove stars with a warning flag in the parameter STARFLAG, which is related to issues with the spectrum, the number of sources is reduced by 54% with respect to the total sample (10 in-plane stars at $R > 24$ kpc instead of 37 without the cut), and the radius for a 3σ detection is $R = 21.8$ kpc (instead of $R = 22.9$ kpc). When this last subsample is combined with only 46% of the sources in APOGEE with LAMOST, we find the presence of disk stars distinct from the halo sources, at $R > 22.8$ kpc at 5σ, $R > 24.7$ kpc at 3σ, and $R > 27.1$ kpc at 2σ. This slight reduction of the maximum radius of the disk is due to the reduction of the number of sources, which makes the detection less significant at a given radius. We may then conclude that our results are not importantly affected by possible misclassified sources, which should introduce noise rather than signal.

This analysis corroborates through statistical spectroscopy the lack of a radial truncation in the stellar disk observed through the fit of star counts out to 30 kpc (LM14). An exponential distribution is also observed for the gas density of the Milky Way without any truncation up to a distance of 40 kpc from the center (Kalberla & Dedes 2008). This does not mean that radial truncations are not possible in spiral galaxies: there are other galaxies in which they are observed (van der Kruit & Searle 1981; Pohlen et al. 2000), but the Milky Way is not one of them.

Acknowledgements. MLC and FGL were supported by the grant AYA2015-66506-P of the Spanish Ministry of Economy and Competitiveness (MINECO). Thanks are given to the anonymous referee for helpful comments and Astrid Peter (language editor of A&A) for the revision of this paper. Guoshoujing Telescope (the Large Sky Area Multi-Object Fiber Spectroscopic Telescope LAMOST) is a National Major Scientific Project built by the Chinese Academy of Sciences. Funding for the project has been provided by the National Development and Reform Commission. LAMOST is operated and managed by the National Astronomical Observatories, Chinese Academy of Sciences. Funding for the Sloan Digital Sky Survey IV has been provided by the Alfred P. Sloan Foundation, the U.S. Department of Energy Office of Science, and the Participating Institutions. SDSS-IV acknowledges support and resources from the Center for High-Performance Computing at the University of Utah. The SDSS web site is www.sdss.org. SDSS-IV is managed by the Astrophysical Research Consortium for the Participating Institutions of the SDSS Collaboration including the Brazilian Participation Group, the Carnegie Institution for Science, Carnegie Mellon University, the Chilean Participation Group, the French Participation Group, Harvard-Smithsonian Center for Astrophysics, Instituto de Astrofísica de Canarias, The Johns Hopkins University, Kavli Institute for the Physics and Mathematics of the Universe (IPMU) / University of Tokyo, Lawrence Berkeley National Laboratory, Leibniz Institut für Astrophysik Potsdam (AIP), Max-Planck-Institut für Astronomie (MPIA Heidelberg), Max-Planck-Institut für Astrophysik (MPA Garching), Max-Planck-Institut für Extraterrestrische Physik (MPE), National Astronomical Observatories of China, New Mexico State University, New York University, University of Notre Dame, Observatário Nacional / MCTI, The Ohio State University, Pennsylvania State University, Shanghai Astronomical Observatory, United Kingdom Participation Group, Universidad Nacional Autónoma de México, University of Arizona, University of Colorado Boulder, University of Oxford, University of Portsmouth, University of Utah, University of Virginia, University of Washington, University of Wisconsin, Vanderbilt University, and Yale University.

References

Abolfathi, B., Aguado, D. S., Aguilar, G., et al. 2017, arXiv:1707.09322
Allende Prieto, C., Fernández-Alvar, E., Schlesinger, K. J., et al. 2014, A&A, 568, id. A7
Amôres, E. B., Robin, A. C., & Reylé, C. 2017, A&A, 602, A67
Bahcall, J. N. & Soneira, R. M. 1980, ApJS, 44, 73
Beers, T. C., & Christlieb, N. 2005, ARA&A, 43, 531
Carlin, J. L., Chao, L., Newberg, H. J., et al. 2015, AJ, 150, 4
Carraro, G., Vázquez, R. A., Costa, E., Perren, G., & Moitinho, A. 2010, ApJ, 718, 683
Feast, M. W., Menzies, J. W., Matsunaga, N., & Whitelock, P. A. 2014, Nature, 509, 342
Feigelson, E. D. & Babu, G. J. 2012, Modern Statistical Methods for Astronomy with R Applications, Cambridge Univ Press, Cambridge (U.K.), ch. 3
Fernández-Alvar, E., Allende Prieto, C., Schlesinger, K. J., et al. 2015, A&A, 577, A81
Freudenreich, H. T., Berriman, G. B., Dwek, E., et al. 1994, ApJ, 429, L69
García Pérez, A. E., Allende Prieto, C., Holtzman, J. A., et al. 2016, AJ, 151, id. 144
Hayden, M. R., Bovy, J., Holtzman, J. A., et al. 2015, ApJ, 808, 132
Holtzman, J. A., et al. 2018, in preparation
Kalberla, P. M. W., & Dedes, L., 2008, A&A, 487, 951
Liu, C., Deng, L. C., Carlin, J. L., et al., 2014, ApJ, 790, 110
Liu, C., Xu, Y., Wan, J.-C., et al. 2017, RAA, 17, 96
López-Corredoira, M., & Molgó, J. 2014, A&A, 567, A106 (LM14)
López-Corredoira, M. Momany, Y. Zaggia, S., & Cabrera-Lavers, A. 2007, A&A, 472, L47
Majewski, S. R., Schiavon, R. P., Frinchaboy, P. M., et al. 2017, AJ, 154, id. 94
McKee, C. F., Parravano, A., & Hollenbach, D. J. 2015, AJ, 814, id. 13
Minniti, D., Saito, R. K., Alonso-García, J., Lucas, P. W., & Hempel, M. 2011, ApJ, 733, L43
Momany, Y. Zaggia, S. R., Gilmore, G., et al., 2006, A&A, 451, 515
Nandakumar, G., Schultheis, M., Hayden, M., Rojas-Arriagada, A., Kordopatis, G., & Haywood, M. 2017, A&A, 606, A97
Pohlen, M., Dettmar, R.-J., & Lütticke, R. 2000, A&A, 357, L1
Porcel, C., Battaner, E., & Jiménez-Vicente, J. 1997, A&A, 322, 103
Reylé, C., Marshall, D. J., Robin, A. C., & Schultheis, M. 2009, A&A, 495, 819
Ruphy, S., Robin, A. C., Epchtein, N., et al. 1996, A&A, 313, L21
Sale, S. E., Drew, J. E., Knigge, C., et al. 2010, MNRAS, 402, 713
Santiago, B. X., Brauer, D. E., Anders, F., et al. 2016, A&A, 585, id. A42
Schultheis, M., Zasowski, G., Allende-Prieto, C., et al. 2014, AJ, 148, id. 24
van der Kruit, P. C., & Searle, L. 1981, A&A, 95, 105
Vaucouleurs, G. de, & Pence, W. D. 1978, AJ, 83, 1163
Xu, Y., Liu, C., Xue, X.-X., et al. 2017, MNRAS, 473, 1244
Wang, J., Shi, J., Pan, K., Chen, B., Zhao, Y., & Wicker, J. 2016, MNRAS, 460, 3179
Wang, Q., Wang, Y., Liu, C., Mao, S., & Long, R. J. 2017, MNRAS, 470, 2949